

Physical properties of circumnuclear ionising clusters. I. NGC 7742

S. Zamora,^{1,2}★† Ángeles I. Díaz,^{1,2}

¹*Departamento de Física Teórica, Universidad Autónoma de Madrid, 28049 Madrid, Spain*

²*CIAFF, Universidad Autónoma de Madrid, 28049 Madrid, Spain*

Accepted 2023 July 03. Received 2023 June 30; in original form 2022 December 22

ABSTRACT

This work aims to derive the physical properties of the CNSFRs in the ring of the face-on spiral NGC 7742 using IFS observations. We have selected 88 individual ionising clusters that power HII regions populating the ring of the galaxy that may have originated in a minor merger event. For the HII regions the rate of Lyman continuum photon emission is between 0.025 and $1.5 \cdot 10^{51}$ which points to these regions being ionised by star clusters. Their electron density, ionisation parameter, filling factor and ionised hydrogen mass show values consistent with those found in other studies of similar regions and their metal abundances as traced by sulphur have been found to be between 0.25 and 2.4 times solar, with most regions showing values slightly below solar. The equivalent temperature of the ionising clusters is relatively low, below 40000 K which is consistent with the high elemental abundances derived. The young stellar population of the clusters has contributions of ionising and non-ionising populations with ages around 5 Ma and 300 Ma respectively. The masses of ionising clusters once corrected for the contribution of underlying non-ionising populations were found to have a mean value of $3.5 \times 10^4 M_{\odot}$, comparable to the mass of ionised gas and about 20 % of the corrected photometric mass.

Key words: galaxies: abundances – galaxies: ISM – galaxies: star clusters: general – galaxies: starburst – ISM: abundances – Nebulae, (ISM:) H II regions – Nebulae

1 INTRODUCTION

Careful determinations of abundance distributions over galaxies at the early stages of their evolution could provide important pieces of information about their formation processes since gas accretion or gas ejection episodes will leave an imprint on these abundance distributions. However, several important caveats exist: (a) the assumption that the ionisation of the gas in inner regions of galaxies is due only to star formation processes; (b) that the star formation modes dominating at high redshifts are similar to those encountered in the local universe. Regarding the first, it is nowadays generally accepted that some connection exists between star formation and activity in galactic nuclei, and young stars appear as one component of the unified model of AGN giving rise to the blue featureless continuum which is observed in Seyfert 2 galaxies where the broad line region is obscured. But regarding the second, that is that the star formation modes dominating at high redshifts are similar to those encountered in the local universe, this might not be the case. Recently, large and massive clumps of star formation have been detected in more than half of the resolved $z > 1$ galaxies in the Hubble UDF (see Elmegreen & Elmegreen 2005). These star-forming

entities are in galaxies at all distances covered by the ACS ($0.07 < z < 5$). They have sizes of about 2 kpc, estimated ages of 10 Ma and masses often larger than $10^8 M_{\odot}$. They are so luminous that they dominate the appearance of their host galaxies. Massive clumps like these are found in galaxies with a variety of morphologies, from somewhat normal ellipticals, spirals, and irregulars, to types not observed locally, including chain galaxies and their face-on counterparts, clump-cluster galaxies.

Interestingly enough these star-forming entities which seem to constitute the star formation mode in galaxies at high redshifts resemble the well known circumnuclear star-forming regions (CNSFRs), a common mode of star formation found close to galactic nuclei. These regions, many of them a few hundred pc in size and showing integrated $H\alpha$ luminosities which overlap with those of HII galaxies (typically higher than $10^{39} \text{ erg s}^{-1}$), seem to be composed of several HII regions ionised by luminous compact stellar clusters whose sizes, as measured from high spatial resolution Hubble Space Telescope (HST) images, are seen to be of only a few pc. These regions are young (age < 10 Ma and massive (up to $2 \times 10^8 M_{\odot}$) (Hägele et al. 2007, 2013). In the UV-B wavebands, they contribute substantially to the emission of the entire nuclear region, even in the presence of an active nucleus (see e.g. Colina et al. 2002). In a galaxy like NGC 3310 the starburst “ring” is the strongest organized source of far-UV (FUV) emission and 30% of the total observed FUV emission is produced within a radius of $10''$. At redshifts of z

★ E-mail: sandra.zamora@uam.es

† PhD fellow of Ministerio de Educación y Ciencia, Spain, BES-2017-080509, CEAL-AL/2017-02

2–3, this structure would be confined to a region 0.2'' in diameter for $\Omega = 1$ and would appear point-like in low-resolution observations. Consequently, in the absence of diagnostic spectroscopy, a high-redshift NGC 3310–like object could be mistaken for an active galactic nucleus (AGN).

CNSFRs in nearby galaxies, being close to the galactic nuclei, are expected to be of high metal abundance. However, detailed long-slit spectroscopic analyses show that most of them have abundances consistent with solar values (Díaz et al. 2007). Also, their ionisation structure as mapped by suitable emission line ratios is more similar to that of HII galaxies than to galactic disc GEHR, pointing to relatively hard ionising sources, not expected at high metallicities. As mentioned above, similar effects have been found for a considerable sample of star-forming galaxies at $1.0 < z < 1.5$ (see e.g. Liu et al. 2008). The answer might be related to the influence of a hidden low luminosity AGN, the presence of shocks in zones of high specific star formation rates, or harder ionizing continuum sources among other possibilities.

The above mentioned work of Díaz et al. (2007) was based on long-slit spectroscopy, which is very time consuming, and involved a few CNSFRs in three selected galaxies with the total number of regions studied amounting to a dozen. Obviously, the best strategy to study the complex star forming regions in circumnuclear rings is the use of Integral Field Spectroscopy (IFS). The Multi-Unit Spectroscopic Explorer (MUSE) available at VLT offers the opportunity to carry out this detailed study program. Typical circumnuclear rings have sizes of less than 1kpc (20 arcsec at a distance of 10 Mpc), hence are easily accommodated in the large field of view of MUSE (1 arcmin²) which also provides the necessary combination of high spatial (0.3 - 0.4 arcsec) and spectral resolution ($R \approx 2000 - 4000$). The use of this technique greatly reduces the observing time and can increase the number of analysed clusters by an order of magnitude. On the other hand, the usually high abundances of the objects involved and their low excitation produce very weak [OIII] lines, difficult to measure with confidence, precluding the use of these lines for the analysis. The extended range of wavelength to the red provided by MUSE allows the use of Sulphur as an alternative abundance and excitation tracer for the characterisation of the HII regions and ionising clusters (Díaz & Zamora 2022, see).

In this first paper we present the study of the physical properties of the CNSFRs in the ring of the face-on galaxy NGC 7742 using MUSE observations publicly available and the full spectral region observed, from 4800 to 9300 Å. NGC 7742 is classified as an SA(r)b galaxy. It has a weakly active nucleus classified as T2/L2 in Ho et al. (1997), that corresponds to a transition object whose spectrum is dominated by emission lines characteristic of both LINER and HII regions. Its morphology is dominated by a nuclear ring which is easily identified by prominent bumps on the luminosity profiles in different photometric bands at galactocentric distance between 9 and 11 arcsec which corresponds to around 1 kpc at the assumed distance of 22 Mpc (Tully & Fisher 1988). The feature shows up most importantly in the U band thus pointing to a star formation origin (Wakamatsu et al. 1996). Apart from the ring, the surface brightness profile can be represented by the combination of two exponential discs and one central bulge (Sil'chenko & Moiseev 2006). The galaxy shows a high degree of circular symmetry at different spatial levels: core, ring, and main body, and hence constitutes a very good case for the study of formation mechanisms of nuclear rings in non-barred galaxies. It is also one of the approximately 10% spirals showing a gaseous counter-rotating disc (Pizzella et al. 2004), that was first reported by de Zeeuw et al. (2002).

The kinematics of gas and stars in the central part of this

Table 1. NGC 7742 global properties.

Galaxy	NGC 7742
RA J2000 (deg) ^a	356.065542
Dec J2000 (deg) ^a	10.767083
Morphological type	SA(r)b
Luminosity Class	LC II
Nuclear type	LINER/HII
z	0.00555
Distance (Mpc) ^b	22.2
Scale (pc/arcsec) ^c	92

^a Skrutskie et al. (2006).

^b Tully & Fisher (1988).

^c Cosmology corrected scale.

galaxy has been studied in detail by Martinsson et al. (2018), also using MUSE data. In their work they have mapped the ring counter-rotation and have found evidence for two distinct stellar populations: the older of them counter-rotates with the gas while the younger one, concentrated to the ring, co-rotates with the gas. They conclude that the ring has been originated in a minor merger event that took place probably 2-3 Ga ago.

The present work is centred in the study of the individual ionising clusters that power the HII regions populating the ring of NGC 7742. The observations on which the work is based are presented in section 2 together with the description of the data reduction; section 3 is devoted to the description of the measurement methods and the data analysis; section 4 presents the results; the discussion is given in section 5 and our final conclusions are in Section 6.

2 OBSERVATIONS AND DATA REDUCTION

In this work we analyse the almost face-on galaxy NGC 7742 that shows a prominent circumnuclear star-forming ring using publicly available observations obtained by the IFS MUSE. Some characteristics of this galaxy are given in Table 1.

The Multi-Unit Spectroscopic Explorer, MUSE (Bacon et al. 2010) is an integral-field spectrograph (IFS) located at the Nasmyth focus of the Very Large Telescope (VLT) on the Unit Telescope 4 (UT4), of the European Southern Observatory (ESO) at Cerro Paranal, Chile. It operates in the visible wavelength range, covering from 4800 Å to 9300 Å with a nominal dispersion of 1.25 Å/pixel with a spectral resolving power from 1770 (at 4800 Å) to 3590 (at 9300 Å) in the blue and red arms respectively. It is composed of 24 integral field units (IFUs) which, in the Wide Field Mode (WFM), provides a field of view (FoV) of 60 arcsec² with a spatial sampling of 0.2 arcsec².

NGC 7742 was observed as part of the first MUSE Science Verification run on 2014 June 22 under ESO Programme 60.A-9301(A) (PI: M. Sarzi). The observing time was split in two exposures of 1800s with an offset of 1 arcsec in declination and a rotation of 90° between observations and with a median seeing of 0.63 arcsec. Offset sky observations were taken before or after the target observations for adequate sky subtraction.

We have used the ESO Phase 3 Data Release. The reduction of the data was performed by the Quality Control Group at ESO in an automated process applying version 0.18.5 of the MUSE pipeline (Weilbacher et al. 2014). They used calibration images taken as part of the standard MUSE calibration plan using different point-

Table 2. Extraction parameters for emission line maps.

Line	λ_c (Å)	$\Delta\lambda$ (Å)	$\Delta\lambda_{left}$ (Å)	$\Delta\lambda_{right}$ (Å)
H α	6563	8	6531.5 - 6539.5	6597.0 - 6605.0
H β	4861	8	4811.0 - 4819.0	4901.0 - 4909.0
[OIII]	5007	15	4902.5 - 4917.5	5092.5 - 5107.5
[NII]	6583	15	6593.5-6608.5	6542.5-6527.5

All wavelengths are in rest frame.

ings of the object. The corrections applied to each exposure were: subtraction of the master-bias, division by a master-flat-field and illumination correction between all slices of the IFU. Corrections for twilight and differential atmospheric refraction were also made. Data were wavelength calibrated, corrected for telluric absorption and sky subtracted using a dedicated offset exposure of 300s. Finally, the data were flux calibrated. The astrometric solution was provided and the data were resampled into a datacube. Finally, the produced individual datacubes were weighted by their respective exposure time and resampled into a single combined one.

We have also used additional data from Hubble Space Telescope (HST) that were acquired on 1995 July 9 with the Wide Field and Planetary Camera 2 (WFPC2) as a part of the program [GTO/wfc 6276](#) (IP: J. Westphal) providing high-resolution images with a spatial resolution of ≈ 0.1 arcsec pixel $^{-1}$ and FoV of 150 arcsec 2 . The data have been obtained from the Hubble Legacy Archive and are organised in 3 exposures of 700 s each in the U broad band obtained with the F336W filter. The reduction of these data has been performed by the Space Telescope Science Institute (STScI) using available calibration files taken for this observation and keeping in mind different dithering positions. The pipeline provides standard calibrations like correction for permanent camera defects, the temperature-dependence of the WF4 detector gain, bias, dark current and flat field corrections, the position-dependent exposure time and the absolute detector efficiency. Additionally, STScI has reprocessed all WFPC2 data including improvements to the time-dependent UV contamination, the variation in the bias level in WF4 and other subtle details.

3 RESULTS AND ANALYSIS

3.1 Emission line and continuum maps

From the observed data cubes we have constructed 2D maps which are presented in Figure 1. For the different emission lines we have assumed a linear behavior of the continuum emission in the region of interest choosing side-bands around each line of a given width. Table 2 give the identification of each line in column 1, its centre wavelength, λ_c in Å in column 2, its width, $\Delta\lambda$, in Å in column 3, and the limits of the two continuum side-bands, in Å in columns 4 and 5. The H α and H β maps have been combined to produce an extinction map. We have also produced maps in two continuum bands of 100 Å width centered at 5400 Å (blue) and 8150 Å (red). All wavelengths are in rest frame.

The two top left panels of Fig. 1 show the spatial distribution of the observed H α and [OIII] fluxes in logarithmic scale. Superimposed on these maps we have represented the contours of HST data from WFC2 in the F336W filter where young star clusters would be more conspicuous. This provides a good comparison between the spatial resolution provided by the two instrumental configurations. The coincidence between the young clusters identified by the HST

contours with the MUSE maps, specially in the H α one ensures that we are actually detecting ionising star clusters. On this H α map the diffuse gas of the circumnuclear ring is also clearly seen. On the other hand, the [OIII] λ 5007 Å emission, traces the different excitation conditions of the ionised gas across the ring. The extinction A_V , in magnitudes, is shown in the top right panel of the figure and has been calculated by adopting the Galactic extinction law of [Miller & Mathews \(1972\)](#), with a specific attenuation of $R_V = 2.97$ and the theoretical ratio $H\alpha/H\beta = 2.87$ from [Osterbrock & Ferland \(2006\)](#) ($n_e = 100$ cm $^{-3}$, $T_e = 10^4$ K, case B recombination) (see also Section 3.3). The distribution of the gas extinction seems to be smooth inside clumps and typically low, with a median value of 1.053 mag in the pixel by pixel analysis peaking around 1.83 mag. The apparently higher extinction values at the edges of the HII regions could be due to the low S/N ratio in the H β emission line that produces an artificially high H α /H β ratio with a large uncertainty. Alternatively, it could be the result of dust created by intense star formation and accumulated by the gas expansion. The two bottom left panels of Fig. 1 show maps of observed continuum fluxes at blue and red wavelengths, 5400Å and 8150Å respectively, on top of which the contours of HST-WFC3 data in the F336W filter. Exponential fits to the stellar surface brightness show two different components with different scale-lengths [Sil'chenko & Moiseev \(2006\)](#). In both maps, HII regions contrast over the galaxy profile and seem to follow the clusters identified in UV emission. Finally, in the bottom right panel we can see the map of the equivalent width (EW) of H α (in Å). All circumnuclear regions present in the ring have $EW(H\alpha) > 20$ Å. This value is consistent with the presence of star formation occurred less than 10 Ma ago.

3.2 HII region selection

Reddening spaxel-by-spaxel analysis has a high uncertainty due to the low S/N of hydrogen H β emission (see the top right panel of Fig. 1). However, we can observe that the reddening is very similar for all ring regions. Thus, we have decided to use the observed H α flux map, i. e. without correcting for reddening, to select ionised regions. In this case, binning is not necessary since a higher S/N is not required and we can preserve the spatial resolution. Furthermore, we do not introduce additional errors in our subsequent analysis. We have selected the spatial extension of the ring on the basis of the spaxel-by-spaxel radial distribution of the observed H α flux shown in the top panel of Figure 2. The area that belongs to the circumnuclear ring can be seen as a bump, in dark-red colour, with H α emission excess over the adjacent continuum, in grey. The limits of the ring are marked on the figure by vertical lines. It has an inner radius of 6 arcsec, 0.75 kpc at the chosen distance of 22.2 Mpc, and an outer radius of 13 arcsec, 1.63 kpc (see Tab. 1). Previous studies report similar radial ring limits (~ 1 kpc; [Comerón et al. 2010](#); [Martinsson et al. 2018](#)).

Our selection method for the HII regions has been made on the basis of the existing `HII_EXPLORER` package, proposed by [Sánchez et al. \(2012\)](#). This program works on a line emission map, usually H α , and detects high intensity clumps, starting with the brightest pixel and adding adjacent ones following specific criteria. It requires several input parameters: the maximum size of the regions, the absolute flux intensity background for all of them (diffuse gas emission level) and the relative flux intensity at maximum to the background for each of the regions. This procedure has already been used in a series of IFS studies, related to CALIFA and MANGA data, but it tends to select regions with similar sizes ([Galbany et al. 2016b](#)). However, HII regions exhibit different sizes, something that

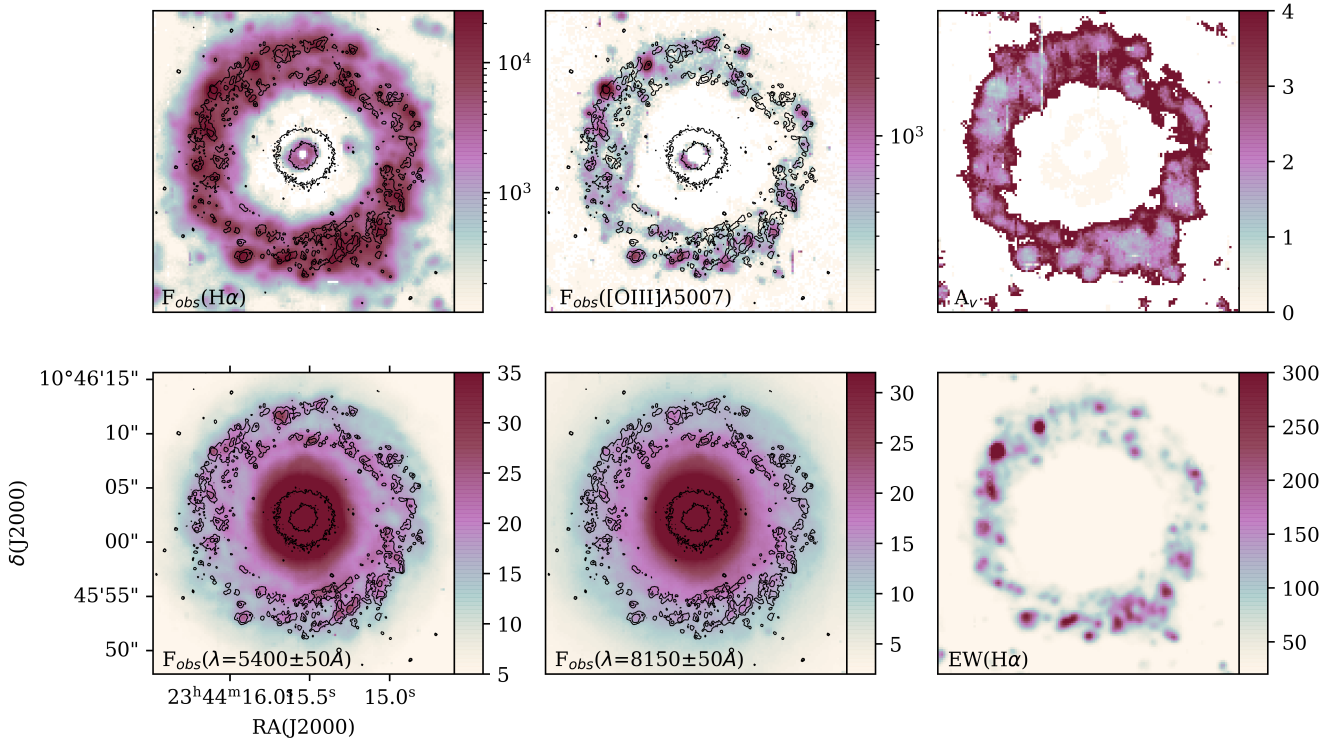


Figure 1. From left to right and top to bottom: Maps of the observed $H\alpha$ and $[OIII]\lambda 5007 \text{ \AA}$ fluxes (in units of $10^{-20} \text{ erg/s/cm}^2$ and logarithmic scale); A_V extinction (in magnitudes); maps for the observed continuum in the blue and red spectral bands (5400 \AA and 8150 \AA respectively, in units of $10^{-17} \text{ erg/s/cm}^2$ and linear scale); and $EW(H\alpha)$ in \AA . Upper and bottom left and centre images show superimposed contours of the HST-UV image which has been described in the text. Orientation is north up, east to the left.

shows up in the higher spatial resolution MUSE data, and hence the $HII_{EXPLORER}$ package is not appropriate. This fact has already been remarked by Galbany et al. (2016a) and here below we describe the implementations we have made to the original package in order to tackle this problem.

We have developed a specific software with the same iterative procedure as the one followed in $HII_{EXPLORER}$ but with some additional requirements. We have selected the maximum extent of regions according to their typical projected size at $z \sim 0.016$ (Gonzalez Delgado & Perez et al. 2011, 500pc), setting a minimum for it according to the point spread function (PSF) value of the input map. We have assumed spherical symmetry and we have modulated the radius of the different regions according to their brightness. We have set an individual flux intensity threshold to each region setting a limit of 10% with respect to the emission of its centre since an asymptotic behavior was found by Díaz et al. (2000a) in $H\alpha$ intensity in their study of CNSFRs. Finally, we have tried different values for the absolute flux intensity background of the complete map adopting that resulting of the best fit of the program, i.e. the one that minimises the dispersion of the spatial residuals in the map.

Apart from the study of the ring HII regions as described above, we have also analysed HII regions external to it for comparison purposes. In order to do that we have ran our segmentation two times, a first one for circumnuclear regions and a second one for those in the outer limit to the ring. The two procedures are slightly different since the absolute flux intensity background is much larger in the further (the diffuse gas emission in the ring is higher). The

second panel of Fig.2 shows the HII regions selected with the use of the methodology described above. Two supernovae, SN 1993R and SN 2014cy, have also been plotted at their respective positions (Treffers et al. 1993; Nishimura 2014, respectively). SN 1993R is a peculiar supernova, similar to SN Ia class 1991bg, but with stronger CaII triplet lines, a weak emission of $[OI]\lambda 630\text{nm}$ and detected in X-Ray emission (Filippenko & Matheson 1993; Bregman et al. 2003). Also, it is superimposed on a very bright HII region which has the highest values of $H\alpha$ emission, $[OIII]\lambda 5007$ emission, A_V and $EW(H\alpha)$ (see Fig. 1). SN 2014cy was classified as SN II and, in the figure, is on top of a region with characteristics similar to the rest of the sample.

Finally, in order to further select data with high quality and also discard failures from the method, we have imposed the following requirements to the integrated spectrum extracted from each selected region: (i) to be certain that the emission has a star formation origin, $EW(H\alpha)$ must be higher than 6 \AA (Cid Fernandes et al. 2010; Sánchez et al. 2015); (ii) to claim the extracted spectrum has physical meaning, the ratio $H\alpha/H\beta$ must be between 2.7 and 6.0, which corresponds to the theoretical values from Osterbrock & Ferland (2006) (assuming an electron density of $n_e = 100 \text{ cm}^{-3}$ and an electron temperature of $T_e = 10^4 \text{ K}$) and an extinction up to 2.3 mag respectively.

At the end of the entire procedure, we have obtained a total of 88 HII regions in the ring and 158 regions outside it. Table 3 shows the position of each HII region in the ring, with respect to that of the galaxy centre, its size and its integrated observed $H\alpha$ emission

Table 3. Selection characteristics for observed CNSFRs. The complete table is available online; here only a part is shown as an example.

Region ID	Area (arcsec ²)	Offsets from galaxy center ^a (arcsec)	F(H α) (10 ⁻¹⁵ erg·s ⁻¹ ·cm ⁻²)
R1*	1.48	-8.4, 6.0	17.621 ± 0.023
R2	1.40	-4.6, 8.2	10.138 ± 0.019
R3	4.28	-8.9, 2.1	19.753 ± 0.053
R4	2.28	-5.8, -9.4	10.306 ± 0.024
R5	1.44	-1.6, -9.6	8.012 ± 0.017
R6	0.20	-2.3, -9.8	1.426 ± 0.003
R7	2.72	7.0, -7.0	11.355 ± 0.026
R8	4.12	8.4, -3.8	15.943 ± 0.044
R9	4.32	2.6, -9.8	16.294 ± 0.040
R10	2.88	3.6, -8.8	14.017 ± 0.030

^a Offsets from centre of the galaxy to the centre of each individual region.

* Region near SN explosion.

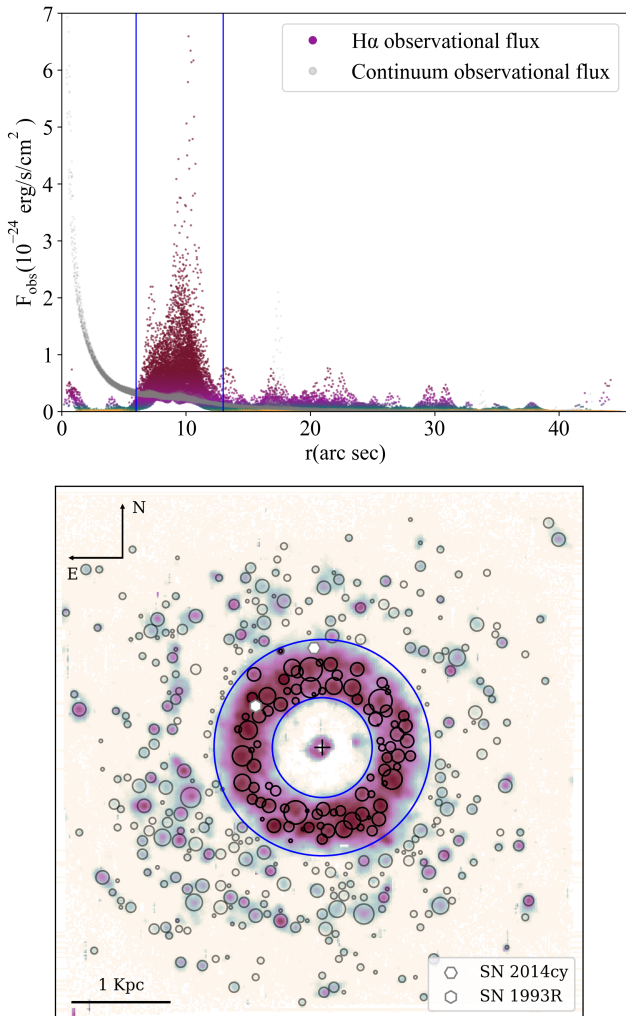


Figure 2. Upper panel: Flux in individual spaxels as a function of radius: continuum near H α with grey dots, integrated flux of this line with colored dots and limits of the ring marked with blue vertical lines. Lower panel: HII regions selected with our segregation program. SN 2014cy and SN 1993R are also plotted (see text). The logarithmic color scale is equivalent with colours presented in the top panel. Orientation is north up, east to the left. The physical scale is represented at the bottom left corner of the map. The limits of the ring are marked with blue circles.

flux. The identification of each region is given in column 1 of the table. SN 1993R lies close to R1.

3.3 Emission line measurements and uncertainties

We have extracted each region spectrum, integrating its corresponding flux in every single aperture produced by the segregation, except in the case of the weak [SIII] λ 6312 Å line for which we have integrated only pixels with S/N > 1.0, as described below. Fig. 3 shows one of these spectra. An underlying stellar population is slightly appreciable in some of our spectra. In order to correct for this effect, we have fitted a Gaussian to the underlying absorption both in the H β and H α lines and subtracted it from the extracted spectra. For the brightest region, this correction has been found to be less than 3% of the observed flux which reflects in a contribution to the measured H β flux within the observational errors.

For each region spectrum, a global continuum has been estimated by fitting a second order polynomial, $F_c(\lambda) = a\lambda^2 + b\lambda + c$ after masking nebular and stellar features. The masks have been built assuming a width of 8Å at each side the central wavelength of the lines involved. To obtain an accurate measure of line fluxes, we have estimated the standard deviation of the residuals of the global continuum fit (σ_c). After subtracting the global continuum, the measurement of fluxes is performed using a single Gaussian fit plus a linear term:

$$f(\lambda) = A_g \cdot e^{-\frac{(\lambda-\lambda_g)^2}{2\sigma_g^2}} + A_c \quad (1)$$

where A_g , λ_g and σ_g are the amplitude, central wavelength and width of the fitted Gaussian. The linear term, A_c , appears as a correction to the global continuum value close to each line. It can take values between $[-\sigma_c, +\sigma_c]$ taking a given value for each measured line. To determine the error of this measurement, and impose quality conditions to it, we have calculated the local standard deviation of the residuals of the Gaussian fit (σ_l) in 30Å around each line. The wavelength window selected for this modelling is adjusted for each line at the first point compatible with σ_c at each side of its central wavelength.

Using this procedure, we have measured the most prominent emission lines in our spectra: H β and H α Balmer lines; [OIII] $\lambda\lambda$ 4959,5007 Å, [NII] $\lambda\lambda$ 6548,84 Å, [SII] $\lambda\lambda$ 6716,31 Å, [ArIII] λ 7136 Å and [SIII] λ 9069 Å forbidden lines. We have taken into account only fluxes of the lines that meet the requirement: $A_g > 3\sigma_l$, thus

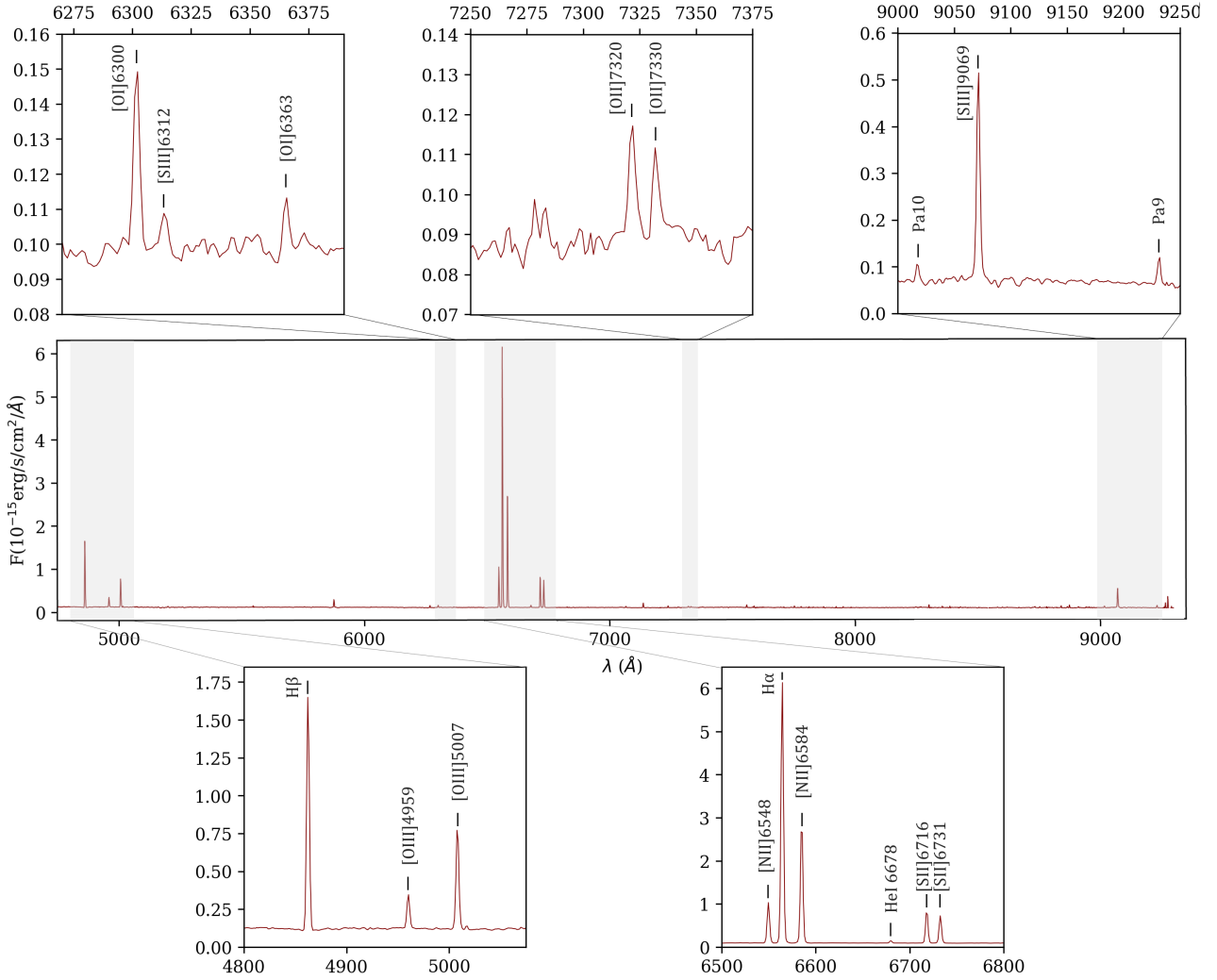


Figure 3. Extracted and reddening corrected spectrum of region R1. Flux is expressed in units of $10^{-15} \text{ erg/s/cm}^2/\text{\AA}$.

discarding the most uncertain values. Additionally, we have measured the weak HeI 6678 \AA line with $A_g > 1\sigma_l$. In the case of [SIII] λ 6312 \AA and [OII] $\lambda\lambda$ 7320,30 \AA , their fluxes have been measured on the spectrum extracted by integration of the pixels where these lines are detected with a tolerance larger than $1\sigma_l$. The [SIII] line has been finally measured with sufficient accuracy in 40 ring HII regions while only 13 regions allowed accurate measurements for the [OII] lines. They have been finally measured with sufficient accuracy in 40 and 13 ring HII regions respectively.

The errors in the observed fluxes have been calculated from the expression given in [Gonzalez-Delgado et al. \(1994\)](#):

$$\Delta[F_\lambda] = \sigma_l \cdot N^{1/2} [1 + EW/(N\Delta)]^{1/2} \quad (2)$$

where $\Delta[F]$ is the error in the line flux, σ_l represents the standard deviation in the local continuum, N is the number of pixels used in the Gaussian fit, Δ is the wavelength dispersion ($1.25 \text{ \AA}/\text{pix}$) and EW is the line equivalent width. The mean value of continuum fluxes, $F_c(\lambda) + A_c$, in the wavelength range $[\lambda_{line} - \sigma_g, \lambda_{line} + \sigma_g]$ has been used to compute this latter value.

Regarding the effects of reddening, we have used a simple screen distribution of the dust and have assumed the same extinction for emission lines and the stellar continuum. The measured line intensities have been corrected using a reddening constant $c(H\beta)$,

derived from the observed $H\alpha/H\beta$ ratio, adopting the Galactic extinction law of [Miller & Mathews \(1972\)](#), with a specific attenuation of $R_v = 2.97$. A theoretical value for the $H\alpha/H\beta$ ratio of 2.87 has been assumed ([Osterbrock & Ferland 2006](#), for $n_e = 100 \text{ cm}^{-3}$ and $T_e = 10^4 \text{ K}$). Given the wavelengths of the lines involved in our study, we have measured their intensities with respect to $H\alpha$ which has a high S/N and is less affected by underlying absorption and reddening effects, thus providing a more precise measurement. Therefore the extinction correction has been applied using the following equation:

$$\log \left(\frac{I(\lambda)}{I(H\alpha)} \right) = \log \left(\frac{F(\lambda)}{F(H\alpha)} \right) + c(H\beta) \cdot (f(\lambda) - f(H\alpha)) \quad (3)$$

where $c(H\beta)$ is the reddening constant, $f(\lambda)$ gives the value of the logarithmic extinction normalised to $H\beta$, and F_λ and I_λ are the observed and corrected emission line fluxes at wavelength λ respectively. Then the $I(\lambda)/I(H\alpha)$ ratio has been translated to $I(\lambda)/I(H\beta)$ assuming the aforementioned value of 2.87 for the theoretical $H\alpha/H\beta$ Balmer decrement. The corresponding errors have been propagated in quadrature.

Table 4 shows, for each selected ring HII region, the reddening

Table 4. Reddening corrected emission line intensities. The complete table is available online; here only a part is shown as an example.

Line	H β	[OIII]	[OIII]	[NII]	H α	[NII]	HeI	[SII]	[SII]	[SIII]	
λ	4861	4959	5007	6548	6563	6584	6678	6717	6731	9069	
f(λ)	0.000	-0.024	-0.035	-0.311	-0.313	-0.316	-0.329	-0.334	-0.336	-0.561	
Region ID	c(H β)	I(H β) ^a	I(λ) ^b								
R1*	0.44 ± 0.01	12.33 ± 0.24	158 ± 3	444 ± 4	438 ± 2	2870 ± 24	1342 ± 3	22 ± 0	334 ± 2	284 ± 2	246 ± 3
R2	0.58 ± 0.01	8.85 ± 0.24	147 ± 4	422 ± 5	461 ± 3	2870 ± 33	1423 ± 5	23 ± 1	367 ± 2	289 ± 2	210 ± 4
R3	0.47 ± 0.02	14.53 ± 0.57	85 ± 6	224 ± 7	421 ± 4	2870 ± 48	1295 ± 6	16 ± 1	460 ± 4	339 ± 3	113 ± 4
R4	0.39 ± 0.01	6.62 ± 0.22	101 ± 5	283 ± 6	442 ± 3	2870 ± 41	1372 ± 6	18 ± 1	525 ± 4	389 ± 3	119 ± 5
R5	0.46 ± 0.01	5.79 ± 0.19	103 ± 5	270 ± 6	439 ± 3	2870 ± 40	1359 ± 5	19 ± 1	367 ± 3	274 ± 3	151 ± 4
R6	0.66 ± 0.02	1.42 ± 0.06	91 ± 7	248 ± 8	442 ± 3	2870 ± 52	1373 ± 6	21 ± 1	364 ± 3	259 ± 2	150 ± 3
R7	0.44 ± 0.02	7.97 ± 0.29	81 ± 6	231 ± 7	387 ± 3	2870 ± 45	1182 ± 5	18 ± 1	415 ± 3	299 ± 3	141 ± 5
R8	0.42 ± 0.02	10.72 ± 0.44	82 ± 7	227 ± 7	411 ± 4	2870 ± 49	1263 ± 7	18 ± 1	435 ± 4	323 ± 4	121 ± 5
R9	0.56 ± 0.02	13.73 ± 0.6	102 ± 8	266 ± 8	419 ± 4	2870 ± 53	1292 ± 6	15 ± 1	445 ± 4	323 ± 3	114 ± 5
R10	0.41 ± 0.01	9.37 ± 0.34	58 ± 5	170 ± 6	367 ± 3	2870 ± 44	1124 ± 5	14 ± 1	399 ± 3	291 ± 3	129 ± 4

^a In units of 10⁻¹⁵ erg/s/cm².^b Values normalized to I(H β) 10⁻³.

* Region near SN explosion.

corrected emission line intensities of strong lines relative to H β , and its corresponding reddening constant.

3.4 Integrated magnitudes

We have calculated integrated fluxes inside the Sloan Digital Sky Survey (SDSS) filters for each region using the following expression (Fukugita et al. 1995):

$$f_{\lambda} = \int_{\Delta\lambda} F(\lambda) \cdot \lambda \cdot T_{\lambda} \cdot d\lambda \quad (4)$$

where T_{λ} denotes the response curves of the r and i bands and $F(\lambda)$ denotes the extracted spectrum of each region. The origin of the additional λ term in this expression lies on the assumption of a photon-counting detector whose response is proportional to the photon-count rate, $\lambda/(hc)$. Before computation, all nebular emission lines present in the spectra have been masked assuming a width of $\pm 8\text{ \AA}$ around the line central wavelength. The spectra have also been corrected for reddening using the $c(\text{H}\beta)$ values calculated from the $\text{H}\alpha/\text{H}\beta$ Balmer decrement (see Sec. 3.3).

The apparent magnitudes of the selected HII regions have been calculated from their integrated fluxes using:

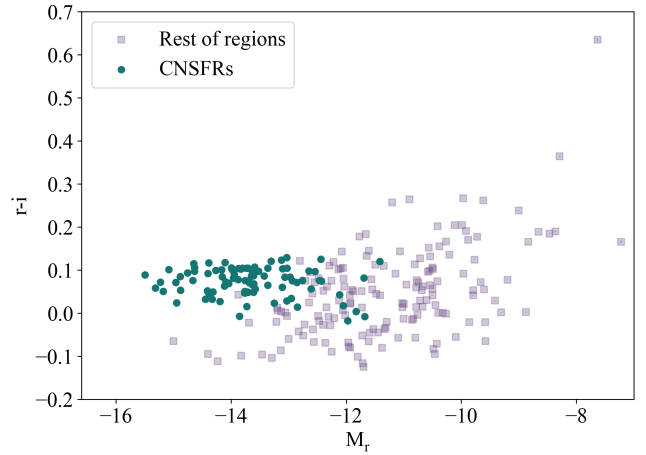
$$m_{\lambda} = -2.5 \cdot \log \left(\frac{f_{\lambda}}{F_0^{\lambda} \cdot \int_{\Delta\lambda} \lambda \cdot T_{\lambda} \cdot d\lambda} \right) \quad (5)$$

where F_0^{λ} is the constant flux density per unit wavelength in the AB System, 2.88637×10^{-9} erg/cm²/s/Å for r band (Zero Point = 21.35 mag) and 1.95711×10^{-9} erg/cm²/s/Å for i band (Zero Point = 21.77 mag). We have assumed a distance of 22.2 Mpc (Tully & Fisher 1988, see Tab. 1) to translate these values into absolute magnitudes. Finally, we have calculated the r-i colours of the regions.

Integrated flux errors have been calculated from the global continuum dispersion and the width of each filter as:

$$\Delta[f_{\lambda}] = \sigma_c \cdot W_{eff} = \sigma_c \cdot \frac{\int T_{\lambda} \cdot d\lambda}{T_{\lambda}^{max}} \quad (6)$$

where $\Delta[f]$ is the error in the integrated flux in one band, σ_c represents the standard deviation in the global continuum flux and T_{λ}

**Figure 4.** Colour-magnitude diagram for HII regions inside (blue dots) and outside (purple squares) the galaxy ring.

is the response curve of each filter. W_{eff} represents the width of a rectangle with the same area covered by the filter and a height equal to its maximum transmission. The calculated errors have been propagated in quadrature for the rest of the derived quantities (apparent magnitudes, absolute magnitudes and r-i colours).

Table 5 shows the integrated magnitudes and derived quantities for each HII region within the ring and lists in columns 1 to 6: (1) the region ID, (2) the apparent magnitude for the i band, (3) the apparent magnitude for the r band, (4) the absolute magnitude for the i band, (5) the absolute magnitude for the r band and (6) the r-i colour.

Figure 4 shows the colour-magnitude diagram of the studied ionised regions that represents a first approach to the properties of their stellar populations underneath. Ring HII regions show r-band luminosities larger than the rest. In regions outside the ring there is a trend of redder r-i colours for lower r-band luminosities that seems to be real given the small size of the observational errors involved (inside the symbols in the graph).

Table 5. Colour and magnitude results. The complete table is available online; here only a part is shown as an example.

Region ID	m_i (mag)	m_r (mag)	M_i (mag)	M_r (mag)	r-i (mag)
R1*	$17.96 \pm (0.23 \times 10^{-4})$	$18.01 \pm (0.15 \times 10^{-4})$	$-13.77 \pm (0.23 \times 10^{-4})$	$-13.72 \pm (0.28 \times 10^{-4})$	$0.049 \pm (0.275 \times 10^{-4})$
R2	$17.92 \pm (0.21 \times 10^{-4})$	$17.97 \pm (0.14 \times 10^{-4})$	$-13.81 \pm (0.21 \times 10^{-4})$	$-13.76 \pm (0.25 \times 10^{-4})$	$0.050 \pm (0.247 \times 10^{-4})$
R3	$16.76 \pm (0.21 \times 10^{-4})$	$16.85 \pm (0.14 \times 10^{-4})$	$-14.97 \pm (0.21 \times 10^{-4})$	$-14.89 \pm (0.25 \times 10^{-4})$	$0.085 \pm (0.254 \times 10^{-4})$
R4	$17.69 \pm (0.26 \times 10^{-4})$	$17.77 \pm (0.18 \times 10^{-4})$	$-14.04 \pm (0.26 \times 10^{-4})$	$-13.96 \pm (0.32 \times 10^{-4})$	$0.081 \pm (0.319 \times 10^{-4})$
R5	$18.00 \pm (0.22 \times 10^{-4})$	$18.08 \pm (0.15 \times 10^{-4})$	$-13.73 \pm (0.22 \times 10^{-4})$	$-13.65 \pm (0.26 \times 10^{-4})$	$0.085 \pm (0.263 \times 10^{-4})$
R6	$19.90 \pm (0.18 \times 10^{-4})$	$19.90 \pm (0.12 \times 10^{-4})$	$-11.83 \pm (0.18 \times 10^{-4})$	$-11.83 \pm (0.22 \times 10^{-4})$	$0.003 \pm (0.215 \times 10^{-4})$
R7	$17.37 \pm (0.24 \times 10^{-4})$	$17.42 \pm (0.16 \times 10^{-4})$	$-14.36 \pm (0.24 \times 10^{-4})$	$-14.31 \pm (0.29 \times 10^{-4})$	$0.049 \pm (0.285 \times 10^{-4})$
R8	$16.88 \pm (0.23 \times 10^{-4})$	$16.97 \pm (0.16 \times 10^{-4})$	$-14.85 \pm (0.23 \times 10^{-4})$	$-14.76 \pm (0.27 \times 10^{-4})$	$0.093 \pm (0.275 \times 10^{-4})$
R9	$16.76 \pm (0.21 \times 10^{-4})$	$16.79 \pm (0.14 \times 10^{-4})$	$-14.97 \pm (0.21 \times 10^{-4})$	$-14.95 \pm (0.25 \times 10^{-4})$	$0.024 \pm (0.249 \times 10^{-4})$
R10	$17.27 \pm (0.22 \times 10^{-4})$	$17.32 \pm (0.15 \times 10^{-4})$	$-14.46 \pm (0.22 \times 10^{-4})$	$-14.41 \pm (0.27 \times 10^{-4})$	$0.051 \pm (0.266 \times 10^{-4})$

* Region near SN explosion.

3.5 Chemical abundance determinations

HII region metallicities have been traced by their sulphur abundances following the methodology described in (Díaz & Zamora 2022), based on red-to-near infrared spectroscopy. The wavelength range used includes the [SIII] λ 6312 Å and [SII] $\lambda\lambda$ 6717,31 Å lines in the red part of the spectrum and the [SIII] $\lambda\lambda$ 9069,9532 Å in the far-red wavelengths. These lines are analogous to the [OII] and [OIII] lines, commonly used to derive oxygen abundances in nebulae. Since sulphur and oxygen are both produced in massive stars both elements are supposed to be proportional to each other. Due to the longer wavelengths of the sulphur lines, reddening effects are less important, which is rather interesting for the study of our observed regions since they are located in the central part of the galaxy. Also, [SII] and [SIII] lines can be measured relative to nearby hydrogen recombination lines ($H\alpha$, P_9) in order to minimise the uncertainties. In addition, sulphur, contrary to oxygen, does not seem to be depleted in diffused clouds (Jenkins 2009) and, due to the lower energies of the involved transitions, the electron temperature sensitive line of [SIII] at λ 6312 Å can be detected and measured up to, at least, solar abundances (Díaz et al. 2007). This methodology is ideal to deal with data from MUSE which do not include the [OII] lines at $\lambda\lambda$ 3727,29 Å. Using this approach, the [SIII] electron temperature, T_e ([SIII]), can be derived using the ratio of the nebular to auroral lines of [SIII] which originate from different upper levels with different excitation energies and hence depend strongly on temperature:

$$R_{S3} = \frac{I(\lambda 9069, 9532)}{I(\lambda 6312)} \quad (7)$$

where $I(\lambda 9069, 9532 \text{ Å})$ denotes the sum of the two near infrared [SIII] lines. MUSE data cover only from 4800 to 9300 Å and therefore do not include the [SIII] λ 9532 Å line; we have used the theoretical relation [SIII] λ 9532 Å / [SIII] λ 9069 Å = 2.44 in order to account for this fact. The following expression has been used (see Díaz & Zamora 2022):

$$t_e([SIII]) = 0.5597 - 1.808 \cdot 10^{-4} R_{S3} + \frac{22.66}{R_{S3}} \quad (8)$$

where $t_e([SIII]) = 10^{-4} \cdot T_e([SIII])[K]$. This expression has been calculated using PyNeb (Luridiana et al. 2015) for values of electron temperatures, T_e ([SIII]), between 5000 K and 25000 K, an electron density of $n_e = 100 \text{ cm}^{-3}$ and the atomic data references listed in Table 6. This equation has a very weak dependence on electron density, increasing by about 3% for values of n_e between 100 and

Table 6. Atomic data sources.

Ionisation state	Collisional strengths	Transition probabilities
S^+	Tayal & Zatsarinny (2010)	Podobedova et al. (2009)
S^{2+}	Hudson et al. (2012)	Podobedova et al. (2009)
O^+	Pradhan et al. (2006)	Zeippen (1982)
	Tayal (2007)	Wiese et al. (1996)
O^{2+}	Aggarwal & Keenan (1999)	Storey & Zeippen (2000)
		Wiese et al. (1996)
Ion	Atomic data	
H	Storey & Hummer (1995)	

1000 cm^{-3} (Pérez-Montero 2017). We have used PyNeb (Luridiana et al. 2015) to calculate the HII region electron densities, n_e , from the [SII] λ 6717 Å / [SII] λ 6731 Å using the atomic coefficients listed in Tab. 6. This ratio has a slight temperature dependence; a value of $T_e = 10000 \text{ K}$ has been assumed. This value is close to the mean value of 9197 K derived from the relation between T_e ([SIII]) and the sulphur abundance given below (see Díaz & Zamora 2022):

$$t_e([SIII]) = (19.226 \pm 0.028) + (-4.7274 \pm 0.0081) \cdot (12 + \log(S/H)) + (0.29879 \pm 0.00058) \cdot (12 + \log(S/H))^2 \quad (9)$$

The derived electron densities of the HII regions within the ring are found to be low and within a narrow range of values centred around 55 cm^{-3} , with a median value of 61 cm^{-3} and a standard deviation of 37 cm^{-3} , in the lower limit for derived densities using these lines. Only eight regions (R1, R2, R16, R19, R51, R54, R66 and R70) have values higher than 100 cm^{-3} , and only three of them (R1, R75 and R66) are significantly different from the median value ($>3\sigma$). About 50% of the regions show electron density values lower than 50 cm^{-3} and hence are undetermined. Mazzuca et al. (2006) also found similar results, concluding that the ring is predominantly populated by clouds of very low electronic density, which are typical of extragalactic HII regions, but lower than those derived for CNSFR (Díaz et al. 2007).

The weak [SIII] λ 6312 Å line has been measured with a S/N higher than 1 in $\sim 45\%$ (40 out of 88) of the HII regions within the ring. For these regions total sulphur abundances have been derived directly using the described method.

In the ring HII regions of our sample, located in the central part of the galaxy and relatively close to its nucleus, most of the sulphur

is expected to be in the form of S^+ and S^{++} . Given the low ionisation potential for sulphur, the contribution by S^0 can be neglected and no contribution from S^{3+} is expected in HII regions of moderate to high metallicity (Díaz & Zamora 2022). Therefore, we have assumed an only zone in which $T_e(S^+) \approx T_e(S^{++}) = T_e([SIII])$, the characteristic electron temperature of the region where both the S^+ and S^{++} S ions overlap and that encompasses almost the whole nebula. Abundances have been calculated using the expressions derived using the PyNeb package using the atomic coefficients listed in Tab. 6 and are given below:

$$12 + \log\left(\frac{S^+}{H^+}\right) = \log\left(\frac{I(\lambda 6717, 31)}{I(H\beta)}\right) + 5.516 + \frac{0.884}{t_e([SIII])} - 0.480 \cdot \log(t_e([SIII])) \quad (10)$$

$$12 + \log\left(\frac{S^{2+}}{H^+}\right) = \log\left(\frac{I(\lambda 9069, 9532)}{I(H\beta)}\right) + 6.059 + \frac{0.608}{t_e([SIII])} - 0.706 \cdot \log(t_e([SIII])) \quad (11)$$

where $I(\lambda 6717, 31 \text{ \AA})$ denotes the sum of the intensities of the two red [SII] lines, $I(\lambda 9069, 9532 \text{ \AA})$ denotes the sum of the intensities of the two near infrared [SIII] lines (i.e. 3.44 times the intensity of the [SIII] λ 9069 \AA line), $I(H\beta)$ denotes the $H\beta$ intensity and $t_e([SIII])$ denotes the electron temperature in units of 10^{-4} K. The errors involved in the fitting procedures used for the derivation of the above expressions are lower than observational errors, thus we have propagated the latter to calculate the final emission line intensity uncertainties.

The total abundance of sulphur has then been calculated as:

$$12 + \log\left(\frac{S}{H}\right) = 12 + \log\left(\frac{S^+}{H^+} + \frac{S^{++}}{H^+}\right) \quad (12)$$

and are given in Table 7 for the 39 HII regions with measurements of the [SIII] λ 6312 \AA line. The table lists in columns 1 to 7: (1) the region ID; (2) the measured [SIII] λ 6312 \AA emission line intensity; (3) the R_{S3} line ratio; (4) the [SIII] electron temperature; (5) and (6) the ionic abundances of S^+ and S^{++} relative to H^+ ; and (7) the total S/H abundance. These regions show sulphur abundance values, that range from 6.52 to 7.49 in units of $12 + \log(S/H)$ ($12 + \log(S/H)_{\odot} = 7.12$, Asplund et al. 2009a), with errors between 0.007 to 0.049 dex.

For the rest of the regions no reliable detection of the [SIII] λ 6312 \AA line could be made and hence we had to rely on empirical calibrations to derive their sulphur abundances. This has been done through the use of the S_{23} parameter, analogous to the commonly used R_{23} for the case of oxygen and can be defined as:

$$S_{23} = \frac{([SII]\lambda 6717, 6731 + [SIII]\lambda 9069, 9532)}{H\alpha} \cdot \frac{H\alpha}{H\beta} \quad (13)$$

This parameter has little dependence on reddening effects or calibration uncertainties since the lines involved can be measured relative to nearby hydrogen recombination lines. Also, the lines are observable even at over-solar abundances given their lower dependence with electron temperature.

A recent calibration of the S_{23} parameter has been presented in Díaz & Zamora (2022) and has the following expression:

$$12 + \log\left(\frac{S}{H}\right) = (6.636 \pm 0.011) + (2.202 \pm 0.050) \cdot \log S_{23} + (1.060 \pm 0.098) \cdot (\log S_{23})^2 \quad (14)$$

The sulphur abundances derived from this calibration for all the objects in our sample are given in Table 8.

4 DISCUSSION

4.1 Ionisation nature

According to Mazzuca et al. (2006), the emission line ratios within the ring are consistent with the predictions of star forming models, although regions near the inner edge of the ring are compatible with the ionisation being produced by shocks or an AGN component, something that could be related to the LINER nature of the galaxy nucleus. Figure 6 shows in the upper panel the classical BPT (Baldwin et al. 1981) diagnostic diagram involving the [NII] λ 6584 / $H\alpha$ and [OIII] λ 5007 / $H\beta$ emission line intensity ratios for the observed regions. The star-forming regions within the ring are shown to lie on the moderate to high metallicity end of the empirical star forming sequence defined by Kauffmann et al. (2003) from observations of a large sample of SDSS emission line galaxies. On the other hand, the data analysed here allow to get some insight on the nature of the nuclear ionised regions. The upper panels of Figure 5 show maps of the central part of NGC 7742 in the [OIII] λ 5007 \AA (left) and [NII] λ 6583 \AA (right) emission line ratios where a small circumnuclear ring at about 200 pc from the galaxy nucleus is seen very distinctively. We have extracted the spectra corresponding to the galaxy nucleus and three of the circumnuclear regions: (a), (b) and (c) and measured their [OIII]/ $H\beta$ and [NII]/ $H\alpha$ ratios. The lower panel of the figure shows the spectrum of region (a) where the large [NII]/ $H\alpha$ characteristic of LINER-type spectra can be seen. Below the optical spectrum we show the Gaussian fits to the $H\beta$, [OIII], $H\alpha$ and the [NII] lines.

The location of the galaxy nucleus and the three circumnuclear selected regions in the BPT diagram marked with a star and purple inverted triangles respectively, lie below and to the right of the yellow line that marks the division between Seyfert and LINER spectra (Schawinski et al. 2007), thus showing that the emission is probably dominated by shocks or an AGN non-thermal component of low activity. Three of our segmented ring regions to the South-East, R85, R86 and R87 (see Fig. 5), lie on the BPT diagram in the zone between the Kauffmann et al. (2003) empirical sequence and the one derived by Kewley et al. (2001) from theoretical models of starburst galaxies and may be somewhat affected by the radiation from the galaxy nucleus; consequently, they have not been considered in our analysis.

The BPT diagram shown is the diagnostic more commonly used, mostly due to the fact that is almost insensitive to reddening effects; however, it is sensitive to the N/O ratio, which is difficult to estimate for nuclear and circumnuclear ionised regions. On the other hand, the near-infrared sulphur emission lines constitute a powerful diagnostic to distinguish between shock and photo-ionisation mechanism (Díaz et al. 1985, see); it is independent of relative abundances and little sensitive to reddening. The two lower panels of Figure 6 show the location of the observed ring HII regions colour coded for sulphur abundance (left) and ionisation parameter (right) where a segregation in these two parameters can clearly be seen. This can be further interpreted with the help

Table 7. Ionic and total sulphur abundances derived by the direct method for the CNSFRs with measured [SIII] λ 6312 Å line intensities. The complete table is available online; here only a part is shown as an example.

Region ID	I([SIII] λ 6312) ^a	R _{S3}	t _e ([SIII]) ^b	12+log(S ⁺ /H ⁺)	12+log(S ⁺⁺ /H ⁺)	12+log(S/H)
R1*	59.2 ± 1.3	176.2 ± 1.6	0.6564 ± 0.0014	6.7413 ± 0.0034	7.0415 ± 0.0098	7.218 ± 0.007
R2	39.6 ± 1.4	161.1 ± 2.8	0.6712 ± 0.0030	6.7331 ± 0.0062	6.9454 ± 0.0180	7.153 ± 0.011
R3	29.1 ± 1.5	193.6 ± 2.9	0.6417 ± 0.0023	6.8886 ± 0.0057	6.7310 ± 0.0212	7.118 ± 0.009
R4	13.6 ± 0.6	199.3 ± 2.4	0.6374 ± 0.0018	6.9577 ± 0.0045	6.7637 ± 0.0196	7.172 ± 0.008
R5	21.4 ± 0.8	140.1 ± 2.2	0.6961 ± 0.0029	6.6678 ± 0.0060	6.7580 ± 0.0189	7.016 ± 0.011
R6	6.5 ± 0.3	113.5 ± 1.5	0.7388 ± 0.0029	6.5699 ± 0.0055	6.6885 ± 0.0166	6.934 ± 0.010
R9	30.1 ± 1.6	178.6 ± 2.4	0.6543 ± 0.0021	6.8409 ± 0.0053	6.7115 ± 0.0212	7.082 ± 0.010
R11	10.4 ± 0.6	236.4 ± 2.7	0.6128 ± 0.0016	6.8517 ± 0.0053	6.8636 ± 0.0203	7.159 ± 0.011
R13	14.8 ± 1.0	320.8 ± 3.0	0.5723 ± 0.0012	7.0735 ± 0.0050	7.1241 ± 0.0181	7.401 ± 0.010
R14	11.9 ± 0.8	172.0 ± 2.7	0.6603 ± 0.0025	6.7984 ± 0.0070	6.7218 ± 0.0247	7.063 ± 0.012

^a In units of 10⁻¹⁸ erg/s/cm².^b In units of 10⁴ K.

* Region near SN explosion.

Table 8. Sulphur abundances of the observed CNSFRs derived by empirical methods. The complete table is available online; here only a part is shown as an example.

Region ID	S23	12+log(S/H)
R1	1.463 ± 0.011	7.029 ± 0.016
R2	1.378 ± 0.014	6.963 ± 0.017
R3	1.187 ± 0.015	6.806 ± 0.018
R4	1.324 ± 0.016	6.920 ± 0.018
R5	1.158 ± 0.015	6.781 ± 0.017
R6	1.140 ± 0.013	6.765 ± 0.016
R7	1.199 ± 0.017	6.817 ± 0.019
R8	1.173 ± 0.018	6.794 ± 0.020
R9	1.160 ± 0.016	6.782 ± 0.018
R10	1.135 ± 0.015	6.761 ± 0.018

of photo-ionisation models. Using the Cloudy (Ferland et al. 2013) code we have computed models for ionisation-bounded nebulae assuming a plane parallel geometry. The computed models have ionisation parameter values $\log(u) = -4.09, -3.46$ and -2.76 and metallicity values $12+\log(\text{S}/\text{H}) = 6.52, 6.89,$ and 7.06 , with the rest of the elements in solar proportions. These parameters cover the range of derived values for the regions. A constant value of the electron density of 100 cm^{-3} has been assumed. The nebula is ionised by a young star cluster synthesised using the PopStar code (Mollá et al. 2009) with Salpeter's IMF (Salpeter 1955) IMF with lower and upper mass limits of 0.85 and $120 M_{\odot}$ respectively, including the nebular continuum in a self-consistent way. We have selected an age of 4.7 Myr to represent the simulated clusters. In the right panel we can see that, within the range of our derived values, regions with high ionisation parameters tend to occupy the lower right zone of the diagram while in the left panel regions with low metallicities lie in the upper left zone. No correlation between these two parameters: ionisation parameter and metallicity, is apparent.

4.2 Characteristics of the observed CNSFRs

The measured $H\alpha$ fluxes for the selected ring HII regions, prior to extinction correction, are between $(226.4 \pm 2.7) \times 10^{-18} \text{ erg/s/cm}^2$ and $(1762.1 \pm 2.3) \times 10^{-17} \text{ erg/s/cm}^2$.

We can compare these results with those obtained by Mazzuca et al. (2008) for this galaxy using narrow band photometry data

obtained with the Auxiliary Port camera of the William Herschel Telescope (WHT) at a spatial resolution comparable to that of the MUSE data. For this comparison we have identified 12 matching regions from Fig. 3 of Mazzuca et al. (2008) and converted our measured fluxes to their tabulated values by adding to them the continuum fluxes in a wavelength band 50 \AA wide centred at $H\alpha$ and the fluxes of the [NII] λ 6548,84 Å emission lines also included within this band. Although a linear correlation seems to exist between both sets of measurements, Mazzuca et al.'s $H\alpha$ fluxes are found to be between ~ 6.8 and ~ 37.6 times our flux values. Only 38 HII regions within the ring were selected by these authors, hence their sizes could be larger than those selected in this work.

In our analysis, we have used a simple screen distribution to the dust and we have assumed that extinction affects lines and stellar continuum in a similar way and we have derived the extinction from the observed Balmer $H\alpha/H\beta$ as compared with the theoretical one. Figure 7 shows that no relation is apparent between the derived extinction values, A_V , in magnitudes with the derived sulphur abundances tracing the global metal content, hence we can conclude that dust is distributed along the line of sight and is not an intrinsic characteristic of each particular region. The fact that the extinction values are very similar both in the regions within the ring and outside it supports our assumption.

The number of hydrogen ionising photons, $Q(H_0)$, in each of the HII regions can be calculated from their extinction corrected $H\alpha$ fluxes, $F(H\alpha)$, once translated into luminosities. Using a local universe typical galaxy distance of 10 Mpc we can write $L(H\alpha)$ in erg s^{-1} as:

$$L(H\alpha) = 1.2 \cdot 10^{38} \left(\frac{F(H\alpha)}{10^{-14}} \right) \left(\frac{D}{10} \right)^2 \quad (15)$$

where $F(H\alpha)$ is expressed in $\text{erg s}^{-1} \text{ cm}^{-2}$ and D is the distance to NGC 7742 which has been taken as 22.2 Mpc (see Tab. 1). The corresponding number of hydrogen ionising photons per second is:

$$Q(H_0) = 7.31 \cdot 10^{11} L(H\alpha) s^{-1} \quad (16)$$

where $L(H\alpha)$ is expressed in erg s^{-1} (see for example, Gonzalez-Delgado et al. 1995). This equation has been derived using the recombination coefficient of the $H\alpha$ line assuming a constant value of electron density of 100 cm^{-3} , a temperature of 10^4 K and case B recombination (Osterbrock & Ferland 2006).

For the ring regions this number is between 1.7×10^{49} and 1.8

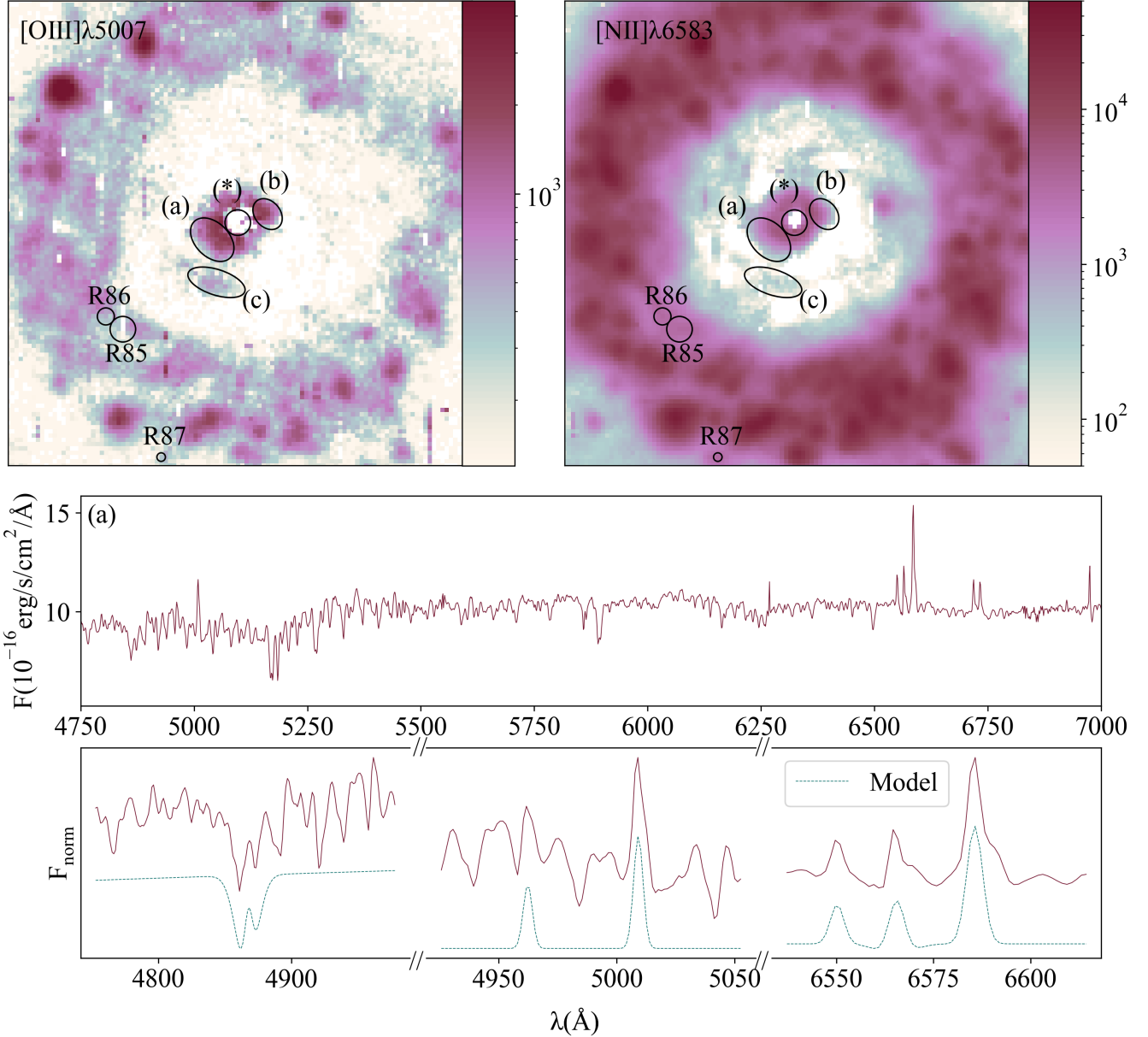


Figure 5. Upper panels: Maps of the observed [OIII] λ 5007 Å (left) and [NII] λ 6583 Å (right) fluxes (in units of 10^{-20} erg/s/cm 2) showing the nuclear environment of NGC 7742. Selected regions are labelled. Bottom panel: Spectrum of region (a) and Gaussian fits to the H β , [OIII], H α and [NII] emission lines.

$\times 10^{51}$ photons-s $^{-1}$, corresponding to logarithmic H α luminosities between 37.36 and 39.40, on the lower side of the distribution found by Álvarez-Álvarez et al. (2015) for a large sample of CNSFRs, but similar to those of the disc HII regions analysed in Castellanos et al. (2002a). According to Mazzuca et al. (2008) disc HII regions in the outer side of the ring have H α luminosities, and therefore a number of ionising photons, lower than the ring regions by about 2 orders of magnitude, implying a higher star formation rate SFR in the galaxy ring as compared to the disc.

On the other hand, the dimensionless ionisation parameter, u , as estimated from the [SII]/[SIII] ratio (Diaz et al. 1991), ranges from 5.5×10^{-5} to 1.1×10^{-3} for the regions within the ring, with a median value of 2.2×10^{-4} . This procedure could be used only for 39 out of 158 of the regions outside the ring. For the rest, the

[SIII] λ 9069 Å line could be measured with too large errors due to poor signal to noise, hence we have calculated the u values from its definition below (see Eq. 17).

The upper left panel of Figure 8 shows these results: HII regions within the ring, with values of $Q(H_0)$ larger than those in the outer side of it, show ionisation parameters centred at about $\log(u) = -3.5$ with a relatively narrow distribution. For the regions outside the ring, the distribution is also centred at the same u value but looks wider extending to lower values. In a previous work analysing a large sample of disc HII regions in more than 200 nearby galaxies from the CALIFA sample, Rodríguez-Baras et al. (2019) found that inner disc regions showing a larger number of Lyman continuum photons showed ionisation parameters lower than their outer disc counterparts. They tentatively attributed this to a selection effect

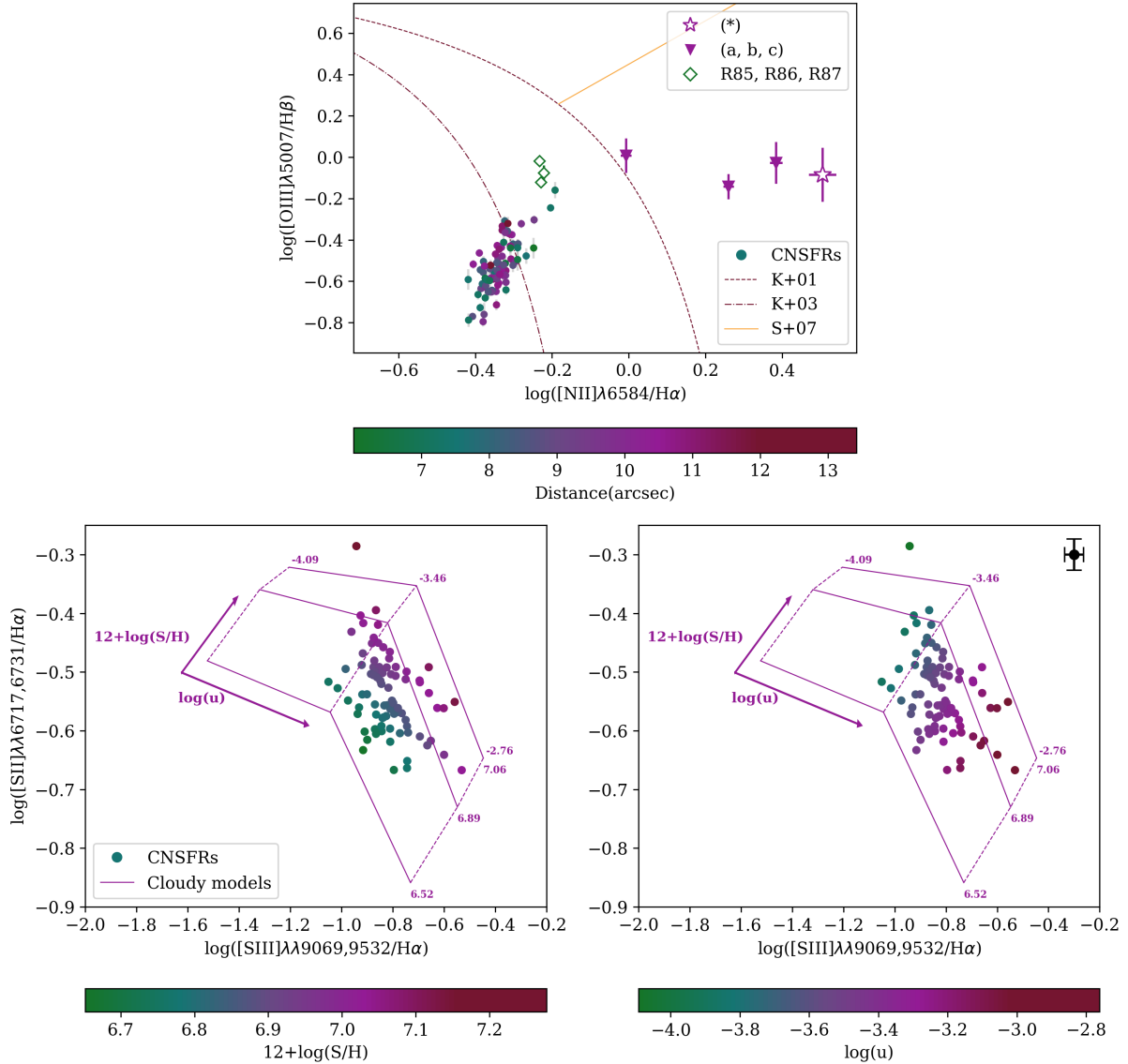


Figure 6. Upper panel: the $[\text{OIII}]/\text{H}\beta$ vs $[\text{NII}]/\text{H}\alpha$ diagnostic diagram for the selected ring HII regions, colour coded according to their distance to the galaxy nucleus. Lower panel, left: the $[\text{SII}]/\text{H}\alpha$ - $[\text{SIII}]/\text{H}\alpha$ diagnostic diagram, colour coded for metallicity. Lower panel, right: The $[\text{SII}]/\text{H}\alpha$ - $[\text{SIII}]/\text{H}\alpha$ diagnostic diagram, colour coded for ionisation parameter. Mean error bars are shown in the upper right corner of the panel. Over-plotted, derived separations between LINER/Seyfert (S+07, Schawinski et al. 2007) and HII regions (K+01 and K+03, Kewley et al. 2001; Kauffmann et al. 2003)

due to the lack of spatial resolution close to the galaxy bulges. However, this was possibly due to the fact that they were missing the population of low $\text{H}\alpha$ luminosity with very noisy spectra.

Some light can be shed on this issue by estimating the filling factors of the observed regions which can be done by comparing their sizes, as estimated using the definition of the ionisation parameter, with the actually measured ones. According to its definition:

$$u = \frac{Q(\text{H}_0)}{4\pi c n_e R^2} \quad (17)$$

where R stands for the radius of the ionised nebulae, provided they have reached their maximum expansion (see Martín-Manjón et al. 2010).

Using the expressions from Castellanos et al. (2002a) we have estimated the angular radii of the observed ring HII regions that have derived electron densities larger than 50 cm^{-3} as:

$$\phi = 0.51 \left(\frac{F(\text{H}\alpha)}{10^{-14}} \right)^{1/2} \left(\frac{u}{10^{-3}} \right)^{-1/2} \left(\frac{n_e}{40} \right)^{-1/2} \quad (18)$$

where ϕ is the angular radius in arcsec. The ionisation parameter predicted radii together with the measured ones, are given in Table 9 and compared in Figure 9. As can be seen from the figure predicted and measured radii are in very good agreement within the errors and are found to be between 0.39 (corresponding to the element resolution) and 1.5 arcsec which correspond to linear values between 34 to 130 pc. This range of values is similar to those found by Díaz et al. (2000b) and Castellanos et al. (2002a) for disc HII regions and is also consistent with the ones calculated by García-Vargas et al. (2013) from PopStar models.

The electron density can be calculated from the $[\text{SII}]\lambda 6717 \text{ \AA}$ / $[\text{SII}]\lambda 6731 \text{ \AA}$ ratio only for $n_e > 50 \text{ cm}^{-3}$. For the regions within

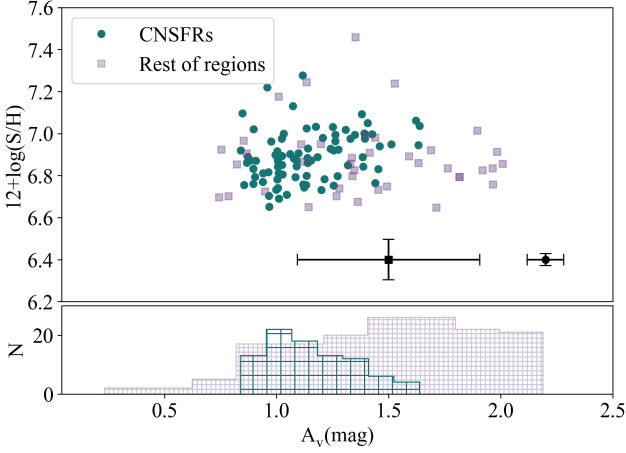


Figure 7. Visual extinction in magnitudes, A_V as a function of sulphur abundance. Average error bars for CNSFRs (right) and the rest of studied regions (left) are shown at the bottom right corner of the panel.

the ring for which only upper limits could be estimated, the electron density has been derived from the observed region sizes as:

$$\frac{n_e}{10} = \left(\frac{F(H\alpha)}{10^{-14}} \right) \left(\frac{10^{-3}}{u} \right) \left(\frac{1}{\phi} \right)^2 \quad (19)$$

Once the ionisation parameter and the angular radius of each observed HII region have been estimated, the filling factor can be derived using the expression:

$$\epsilon = 0.165 \left(\frac{10^{-14}}{F(H\alpha)} \right) \left(\frac{u}{10^{-3}} \right)^2 \left(\frac{1}{\phi} \right) \left(\frac{10}{D} \right) \quad (20)$$

(see Díaz et al. 1991). The Filling factors for the ring HII regions are low, ranging from $(7.7 \pm 1.5) \times 10^{-4}$ to 0.45 ± 0.15 , with a mean value of 0.043. These values are similar to those estimated for high metallicity disc HII regions (between 0.008 and 0.52 Díaz et al. 1991; Díaz et al. 2000b; Castellanos et al. 2002a) and CNSFRs (1×10^{-3} to 6×10^{-4} Díaz et al. 2007).

Finally, the mass of ionised hydrogen, in solar masses, can be derived as (see Díaz et al. 1991):

$$M(HII) = 2.69 \times 10^4 \left(\frac{u}{10^{-3}} \right) \phi^2 \left(\frac{D}{10} \right)^2 \quad (21)$$

These values range from $(1.77 \pm 0.55) \times 10^3 M_\odot$ to $(1.08 \pm 0.16) \times 10^5 M_\odot$, with a mean value of $3.07 \times 10^4 M_\odot$ for the HII regions within the ring and are similar to what is found in disc HII regions.

The bottom panels of Figure 8 show, in panels from left to right, the distribution of electron density, filling factor and ionised hydrogen mass for the ring HII regions as compared with the ones outside the ring. In general, although the electron density shows similar distributions in the two HII region populations, regions within the ring seem to be more diffuse and showing lower filling factors than the regions outside the ring. Given that the size distribution of these latter regions is concentrated around a smaller mean value, this result is expected (Cedr s et al. 2013). Exception is made of a population of outside ring HII regions with low $H\alpha$ luminosity and high filling factor that may correspond to regions ionised by a single star (Vacca et al. 1996).

Tab. 9 shows the characteristics of each HII region within the ring and lists in column 1 to 9: (1) the region ID; (2) the extinction corrected $H\alpha$ luminosity; (3) the number of hydrogen ionising photons; (4) the ionisation parameter; (5) the estimated angular radius; (6) the measured linear radius; (7) the electron density; (8) the filling factor; and (9) the mass of ionised hydrogen.

4.3 Chemical abundances

4.3.1 Sulphur abundance determinations

Reliable measurements of the weak electron temperature sensitive [SIII] line at $\lambda 6312 \text{ \AA}$ have been obtained for 38 ring HII regions out of the 88 originally selected; for these regions sulphur abundances have been derived by the direct method described in section 3.5 and their distribution can be seen in Figure 11 as the histogram filled with oblique lines. Total sulphur abundances are between 6.525 ± 0.007 and 7.50 ± 0.01 in units of $12+\log(S/H)$, that is, between 0.25 and 2.40 times the solar value with a median value of 7.01, slightly below solar. The two ionic species present, S^+ and S^{++} , contribute approximately 50% each to the total abundance.

For the rest of the regions, we have resorted to the empirical calibration by the S_{23} parameter as described in section 3.5 which is single valued up to, at least, solar metallicity. This calibration is shown in Figure 10 where red and blue contours correspond to data for disc HII regions and HII galaxies respectively. Superimposed are the directly derived abundances for the 38 analysed regions with measurements of the [SIII] $\lambda 6312 \text{ \AA}$ line, shown by green stars, and data on regions classified as circumnuclear in the literature as labelled in the figure (Pastoriza et al. 1993; Gonzalez-Delgado et al. 1995, from NGC 3310, NGC 7714 respectively) and are all found to lie at the tip of the curve. The yellow triangle shows the position of HII region 11 from M83 observed by Bresolin et al. (2005). This region is also part of the sample analysed by D az & Zamora (2022) and its derived sulphur abundance is in full agreement with the results of the former authors although the ionisation structure is slightly different.

We have therefore considered jointly the sulphur abundances derived by the two methods. Their distribution can be seen in Figure 11 as the histogram filled with vertical lines. We can see that sulphur abundances derived by the direct method look higher than those calculated from S_{23} parameter calibration. This might reflect the fact that, as in the case of the R_{23} parameter, along the low branch of the calibration the intensity of the [SIII] nebular lines increases with metallicity reaching its maximum at the point where the cooling starts to be dominated by sulphur (about two times the solar value), where the calibration bends to lower values of S_{23} starting to show its bi-valued nature (see Fig. of P rez-Montero & D az 2005). In those cases our empirically derived sulphur abundances could be somewhat underestimated.

4.3.2 The S/O abundance

For 13 regions out of the 88 selected within the ring the [OII] $\lambda\lambda 7320,30 \text{ \AA}$ emission lines have been detected and measured, and 10 of them also show the [SIII] $\lambda 6312 \text{ \AA}$ line. For those 10 regions it was possible to derive the O^+/H^+ ionic abundance. We have assumed an only zone in which $T_e(O^+) \approx T_e(S^{++}) = T_e([SIII])$, $n_e = 100 \text{ cm}^{-3}$ and we have used the following equation derived using the PyNeb package (Luridiana et al. 2015) and the atomic coefficients listed in Tab. 6:

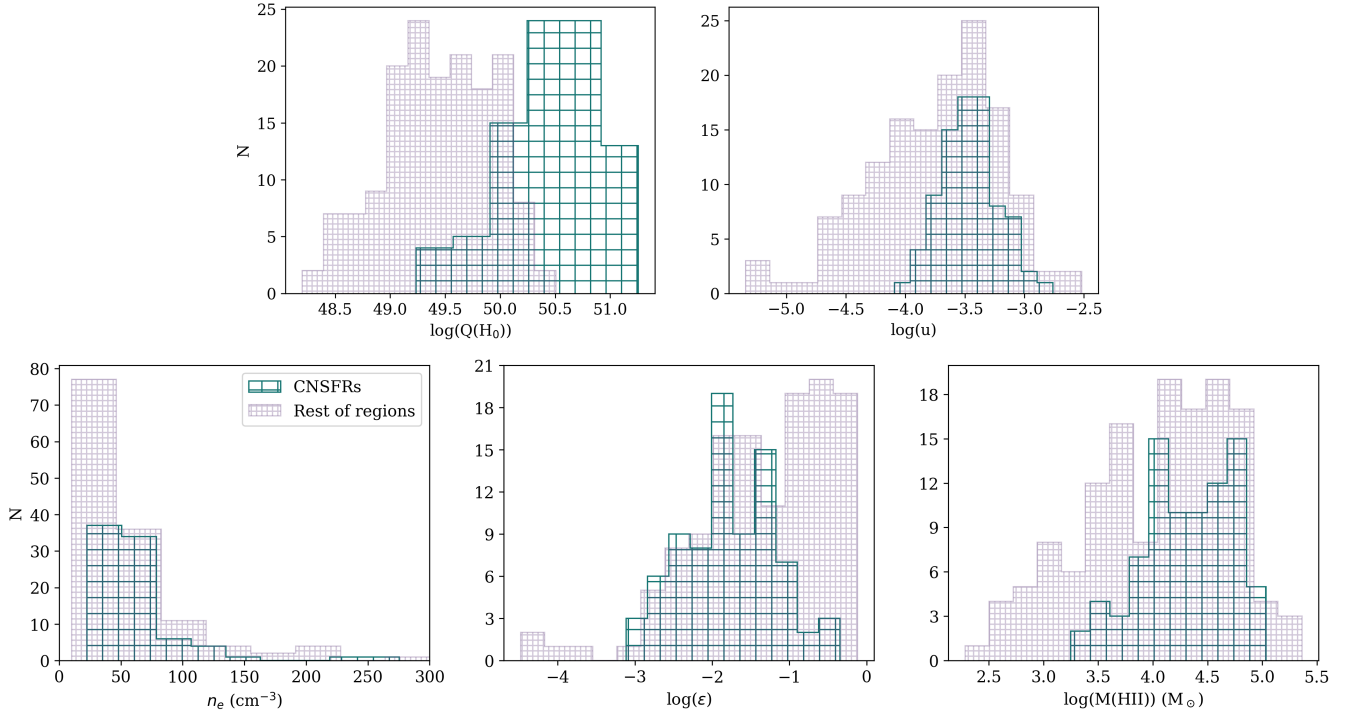


Figure 8. The different histograms in the figure show for the ring HII regions, in green, and regions outside, in purple, the distributions of: the number of hydrogen ionising photons (upper left), the ionisation parameter (upper right), the electron density (bottom left), the filling factor (bottom centre) and the mass of ionised hydrogen (bottom right).

Table 9. Characteristics of the observed CNSFRs. The complete table is available online; here only a part is shown as an example.

Region ID	$L(H\alpha)$ (erg s^{-1})	$Q(H_0)$ (photons s^{-1})	$\log(u)$	ϕ (arcsec)	R (arcsec)	n_e (cm^{-3})	$\log(\epsilon)$	M(HII) (M_\odot)
R1	$(208.8 \pm 4.1) \times 10^{37}$	$(152.8 \pm 3.0) \times 10^{49}$	-2.761 ± 0.009	0.31 ± 0.03	0.69 ± 0.05	224 ± 48	-1.04 ± 0.04	$(10.8 \pm 1.6) \times 10^4$
R2	$(15.0 \pm 1.2) \times 10^{38}$	$(109.7 \pm 3.0) \times 10^{49}$	-2.920 ± 0.014	0.41 ± 0.05	0.67 ± 0.05	130 ± 29	-1.20 ± 0.04	$(7.1 \pm 1.1) \times 10^4$
R3	$(24.6 \pm 2.0) \times 10^{38}$	$(180.0 \pm 7.1) \times 10^{49}$	-3.518 ± 0.028	1.52 ± 0.20	1.17 ± 0.05	62 ± 16	-2.85 ± 0.06	$(54.8 \pm 5.8) \times 10^3$
R4	$(112.0 \pm 9.0) \times 10^{37}$	$(82.0 \pm 2.8) \times 10^{49}$	-3.575 ± 0.028	1.06 ± 0.12	0.85 ± 0.05	66 ± 15	-2.49 ± 0.06	$(25.6 \pm 3.4) \times 10^3$
R5	$(98.1 \pm 7.8) \times 10^{37}$	$(71.8 \pm 2.4) \times 10^{49}$	-3.144 ± 0.020	0.57 ± 0.07	0.68 ± 0.05	75 ± 18	-1.47 ± 0.05	$(43.6 \pm 6.8) \times 10^3$
R6	$(24.0 \pm 2.0) \times 10^{37}$	$(175.5 \pm 7.5) \times 10^{48}$	-3.125 ± 0.017	-	0.25 ± 0.05	89 ± 36	-0.39 ± 0.09	$(6.3 \pm 2.5) \times 10^3$
R7	$(13.5 \pm 1.1) \times 10^{38}$	$(98.7 \pm 3.6) \times 10^{49}$	-3.272 ± 0.025	-	0.93 ± 0.05	39 ± 14	-2.00 ± 0.06	$(61.4 \pm 7.5) \times 10^3$
R8	$(18.1 \pm 1.5) \times 10^{38}$	$(132.8 \pm 5.4) \times 10^{49}$	-3.429 ± 0.031	1.11 ± 0.16	1.15 ± 0.05	70 ± 19	-2.53 ± 0.07	$(64.7 \pm 7.3) \times 10^3$
R9	$(23.2 \pm 2.0) \times 10^{38}$	$(170.1 \pm 7.4) \times 10^{49}$	-3.481 ± 0.030	-	1.17 ± 0.05	48 ± 13	-2.76 ± 0.06	$(60.2 \pm 6.6) \times 10^3$
R10	$(15.9 \pm 1.3) \times 10^{38}$	$(116.1 \pm 4.2) \times 10^{49}$	-3.311 ± 0.024	1.06 ± 0.13	0.96 ± 0.05	51 ± 12	-2.16 ± 0.06	$(59.4 \pm 7.0) \times 10^3$

$$12 + \log\left(\frac{O^+}{H^+}\right) = \log\left(\frac{I(\lambda 7320, 30)}{I(H\beta)}\right) + 6.952 + \frac{2.433}{t_e([SIII])} - 0.571 \cdot \log(t_e([SIII])) \quad (22)$$

The [OII] auroral line intensities might present some contribution by recombination emission that can be estimated as shown in Liu et al. (2001):

$$\left[\frac{I(\lambda 7320 + \lambda 7330)}{H\beta}\right]_R = 9.36 \cdot t_e^{0.44} \frac{O^{++}}{H^+} \quad (23)$$

where t_e is the temperature of the O^+ ion in units of 10^4 K and takes values between 0.5 and 1.0 ($T_e = 5000 - 10000$ K).

For our ring regions this contribution takes values from 0.00016 to 0.0011 and represents between 1.5% and 4.5 % of the emission line intensity, within measurement uncertainties.

The O^{++}/H^+ abundance ratios have been calculated using the expression:

$$12 + \log\left(\frac{O^{++}}{H^+}\right) = \log\left(\frac{I(\lambda 4959 + \lambda 5007)}{I(H\beta)}\right) + 6.249 + \frac{1.184}{t_e([OIII])} - 0.708 \cdot \log(t_e([OIII])) \quad (24)$$

also derived using PyNeb (Luridiana et al. 2015) and the atomic coefficients listed in Tab. 6.

We have assumed that the temperature of the region where the O^{++} ion is originating, $T_e([OIII])$, can be derived from

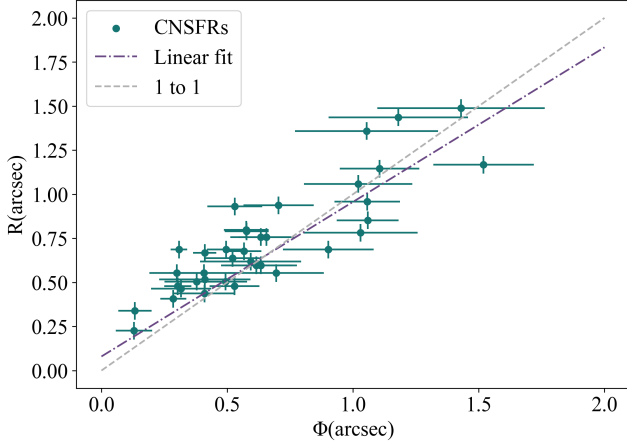


Figure 9. The ionisation derived angular radius against the angular radius measured from the HII region segmentation (see Sec. 3.2).

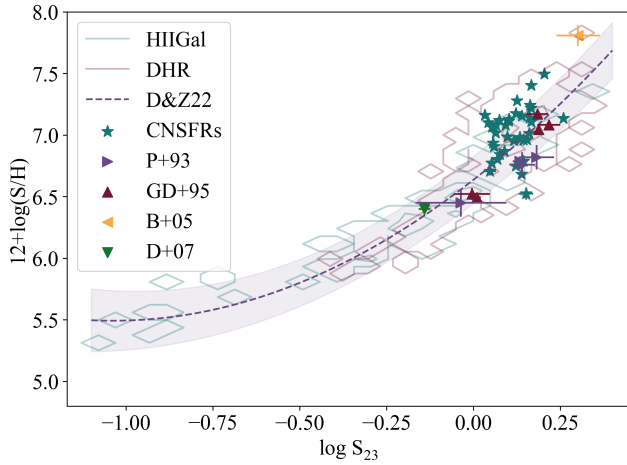


Figure 10. The S_{23} abundance calibration from Díaz & Zamora (2022). Red contours correspond to disc HII regions while blue contours correspond to HII galaxies. Green stars show the values found for the 38 HII regions within the galaxy ring with the $[SIII]\lambda 6312 \text{ \AA}$ line measured. Observational errors for these data are inside the symbols in the graph. Circumnuclear regions from the works by Pastoriza et al. (1993, P+93), Gonzalez-Delgado et al. (1995, GD+95) and Bresolin et al. (2005, B+05) are also shown as labelled in the figure.

$T_e([SIII])$. Figure 12 shows data from Díaz & Zamora (2022) for disc HII regions and HII galaxies (contours in red and blue respectively). Superimposed are different $T_e([OIII]) - T_e([SIII])$ relations proposed in the literature (see Garnett 1992; Pérez-Montero & Díaz 2005; Hägele et al. 2006) as well as other circumnuclear regions with direct determination of these two temperatures (Pastoriza et al. 1993; Gonzalez-Delgado et al. 1995). For high abundances the difference between the plotted relations increases and for $T_e([OIII]) = 5000 \text{ K}$, $T_e([SIII])$ varies from 2740 K to 5850 K for those given by Hägele et al. (2006) and Garnett (1992) respectively. Due to these differences and for consistency with the present work, we have decided to fit the data from Díaz & Zamora (2022) and we have obtained and used the following equation:

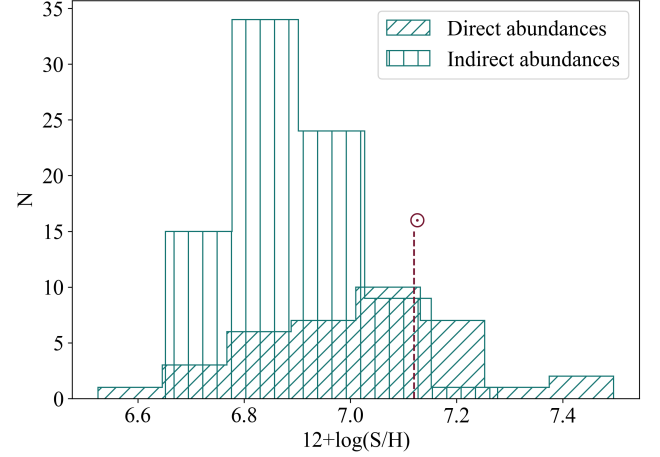


Figure 11. Distribution of the total sulphur abundances for the ring HII regions. The dashed line corresponds to the solar value ($12+\log(S/H)_{\odot} = 7.12$, Asplund et al. 2009a).

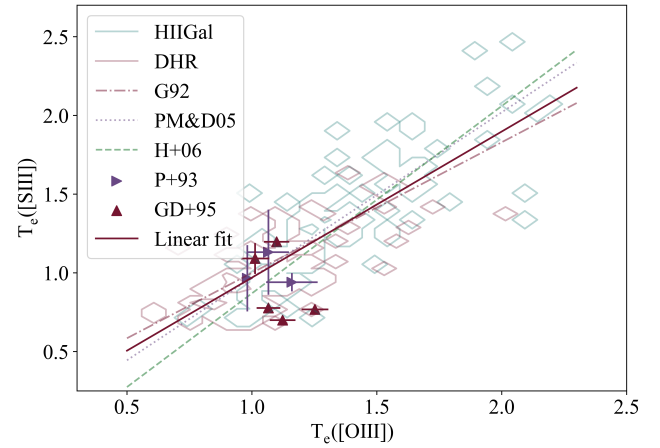


Figure 12. The $T_e([SIII]) - T_e([OIII])$ relation derived by different authors (Garnett 1992; Pérez-Montero & Díaz 2005; Hägele et al. 2006, (G92), (PM&D05) and (H+06) respectively). Red and blue contours are from disc HII regions and HII galaxies data from Díaz & Zamora (2022) respectively. Triangles are electron temperatures measured for CNSFRs from Pastoriza et al. (1993, P+93) and Gonzalez-Delgado et al. (1995, GD+95).

$$t_e([SIII]) = (0.928 \pm 0.053) \cdot t_e([OIII]) + (0.042 \pm 0.057) \quad (25)$$

The total abundance of oxygen has then been calculated as:

$$12 + \log\left(\frac{O}{H}\right) = 12 + \log\left(\frac{O^+}{H^+} + \frac{O^{++}}{H^+}\right) \quad (26)$$

Table 10 shows the oxygen ionic and total abundances and the relative sulphur to oxygen abundance for the 10 regions referred above and lists in column 1 to 8: (1) the region ID; (2,3) the $[OII]\lambda\lambda 7320,30 \text{ \AA}$ auroral lines fluxes and its recombination emission correction; (4) the temperature of the O^{++} ion; (5,6) the ionic oxygen abundances; (7) the total oxygen abundance in units of $12+\log(O/H)$; and (8) the relative sulphur to oxygen abundance in units of $\log(S/O)$. The derived total oxygen abundances, $12+\log(O/H)$, are found to be between 8.16 and 9.5 (mean value of 8.84), corresponding to 0.30

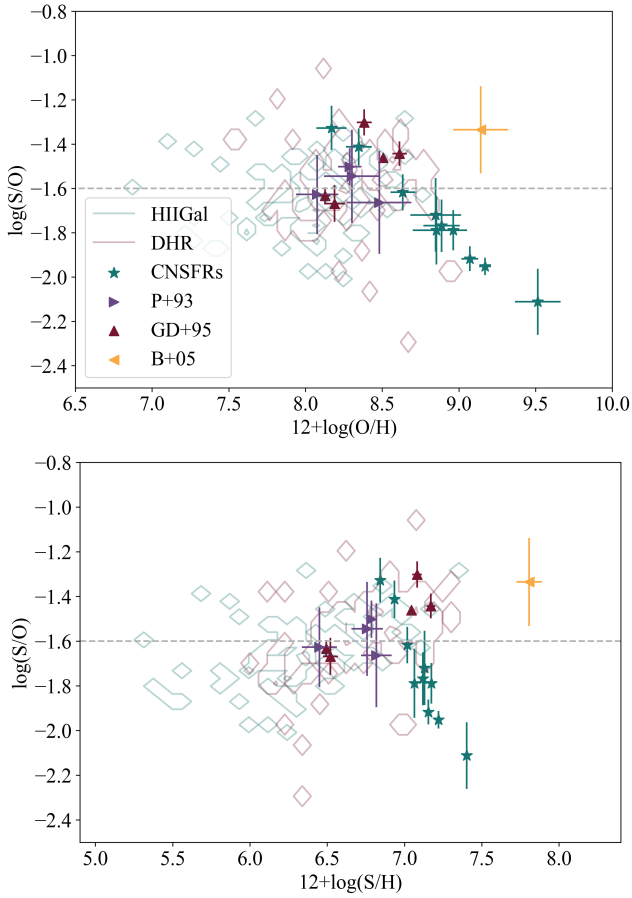


Figure 13. S/O relation against the total abundances of oxygen (upper panel) and sulphur (lower panel) for regions included in Table 10 (green stars) and data from the literature as labelled (Pastoriza et al. 1993; Gonzalez-Delgado et al. 1995; Bresolin et al. 2005, (P+93), (GD+95) and (B+05) respectively). The black dashed line in each panel marks the solar S/O ratio.

and 6.46 times solar ($12+\log(\text{O}/\text{H})_{\odot} = 8.69$, Asplund et al. 2009b), this latter value having a rather high error (± 0.15). For region R42, that shows the highest directly derived sulphur abundance, the [OIII] auroral lines are not detected. The second highest sulphur abundance, $12+\log(\text{S}/\text{H}) = 7.40$ (~ 2 times the solar value) is found for region R13 which also shows the highest value of the oxygen abundance. For all these regions very high values of the O^+/O ionic fraction have been found, between 87% and 95% with a mean value of 92%. Similar ratios have been reported for other high metallicity objects: circumnuclear regions NGC 7714-A and NGC 7714-N110 with ratios $\sim 92\%$ (Gonzalez-Delgado et al. 1995) and region NGC 5236-R11 with a value of 92% (Bresolin et al. 2005). This could be partly due to the highest metallicity regions being ionised by metal rich stars, relatively cool, thus implying a certain lack of O^+ ionising photons decreasing the [OIII] emission line intensity and increasing the [OII] one (e.g. Shields & Searle 1978).

In order to compare our results with other circumnuclear regions from the literature (Pastoriza et al. 1993; Gonzalez-Delgado et al. 1995; Díaz et al. 2007; Bresolin et al. 2005) we have used published emission line measurements and calculated their abundances following the analysis proposed in this work. The O^+/H^+ has been determined from the [OII] $\lambda\lambda$ 3727,29 Å lines and the equation given in Díaz & Zamora (2022). For a few objects we could verify that

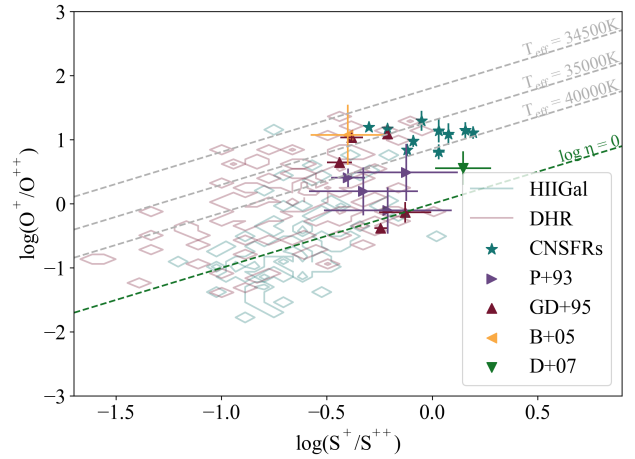


Figure 14. Relation between the ionic ratios of oxygen and sulphur for the objects included in Table 10 (green stars) and data from the literature. Red and blue contours correspond to disc HII regions and HII galaxies respectively from Díaz & Zamora (2022). Circumnuclear regions are from Pastoriza et al. (1993) (P+93), Gonzalez-Delgado et al. (1995) (GD+95), Bresolin et al. (2005) (B+05) and Díaz et al. (2007) (D+07).

O^+/H^+ ratios calculated using the blue and red lines of [OII] are compatible within the errors.

Finally, we have calculated the S/O ratios that are plotted in Figure 13 as a function of both sulphur and oxygen abundance in the upper and lower panel respectively. Both graphs show a clear tendency: lower S/O ratios for higher metallicities, for abundances larger than solar. This effect has already been noticed in other works (Díaz et al. 1991; Christensen et al. 1997; Garnett 2002; Vermeij & van der Hulst 2002; Pilyugin et al. 2006; Díaz & Zamora 2022). This could be due to an overestimation of the derived oxygen total abundances. In fact, as shown by Stasińska (2005) for metallicities larger than solar, directly derived oxygen abundances using photoionisation models deviate greatly from input abundances. However, if this is not the case, the observed S/O lower values for high metallicity regions should be explained almost only by stellar nucleosynthesis (Tosi 1988).

4.4 Ionising cluster properties

The temperature of the ionising stars can be mapped using the η parameter defined by Vilchez & Pagel (1988) as:

$$\eta = \frac{\text{O}^+/\text{O}^{++}}{\text{S}^+/\text{S}^{++}} \quad (27)$$

We can calculate this parameter for only 10 ring HII regions (see Sec. 4.3) and their logarithmic values are between 0.78 ± 0.12 and 1.498 ± 0.043 , on the higher side of the distribution found by Gonzalez-Delgado et al. (1995). A direct relation seems to exist between this parameter and the metallicity for a given region: η is greater (and therefore the temperature of the ionising stars is lower) for regions with higher abundances. This behaviour has already been reported for a sample of HII galaxies by Kehrig et al. (2006, and references therein) and for a large sample of HII galaxies and HII regions of different metallicity by Díaz & Zamora (2022). On the theoretical side it was already introduced by McGaugh (1991) as a moderator in the empirical calibration of the R_{23} parameter.

Fig. 14 shows the relationship between the ionic ratios S^+/S^{++} and O^+/O^{++} for our ring regions and for other circumnuclear regions

Table 10. Oxygen abundances and sulphur to oxygen ratios for the observed CNSFRs.

Region ID	[OII] $\lambda\lambda$ 7320,30/H β ^a	[I(λ 7320,30)/H β] _R ^a	t _e ([OIII]) ^b	12+log(O ⁺ /H ⁺)	12+log(O ⁺⁺ /H ⁺)	12+log(O/H)	log(S/O)
R1*	23.9 ± 2.2	0.69	0.661 ± 0.072	9.145 ± 0.041	7.946 ± 0.009	9.171 ± 0.039	-1.952 ± 0.039
R2	23.1 ± 3.0	0.58	0.677 ± 0.073	9.043 ± 0.059	7.872 ± 0.017	9.072 ± 0.055	-1.917 ± 0.056
R3	10.0 ± 2.9	0.39	0.646 ± 0.072	8.858 ± 0.126	7.708 ± 0.019	8.888 ± 0.118	-1.768 ± 0.118
R4	11.1 ± 2.5	0.50	0.641 ± 0.072	8.931 ± 0.097	7.818 ± 0.014	8.963 ± 0.090	-1.789 ± 0.090
R5	11.3 ± 2.3	0.32	0.704 ± 0.073	8.592 ± 0.090	7.610 ± 0.018	8.635 ± 0.081	-1.617 ± 0.082
R6	9.3 ± 2.0	0.23	0.750 ± 0.075	8.290 ± 0.095	7.447 ± 0.019	8.348 ± 0.084	-1.412 ± 0.084
R13	14.0 ± 5.0	1.14	0.571 ± 0.070	9.493 ± 0.156	8.194 ± 0.015	9.514 ± 0.148	-2.112 ± 0.149
R14	11.9 ± 4.6	0.42	0.666 ± 0.072	8.819 ± 0.167	7.728 ± 0.022	8.853 ± 0.154	-1.789 ± 0.155
R17	11.0 ± 2.8	0.17	0.813 ± 0.077	8.107 ± 0.114	7.294 ± 0.024	8.169 ± 0.099	-1.327 ± 0.100
R26	11.0 ± 4.5	0.37	0.660 ± 0.072	8.818 ± 0.178	7.678 ± 0.024	8.849 ± 0.166	-1.720 ± 0.166

^a Values normalized to I(H β) 10⁻³.^b In units of 10⁴ K.

* Region near SN explosion.

from the literature (Pastoriza et al. 1993; Gonzalez-Delgado et al. 1995; Díaz et al. 2007; Bresolin et al. 2005). Superimposed are dotted diagonal lines which show the location of ionised regions with constant values of η . These values have been correlated with stellar effective temperatures of stars using the Cloudy code (Ferland et al. 2013, log(u) = -4.0 - -2.5, Z_⊙, n_e = 100 cm⁻³) with stellar atmospheres from Mihalas (1978, non-LTE models for B and O stars, log(g) = 4 and T_{eff} from 30000 K to 55000 K). Our circumnuclear regions are located at the high end of S⁺/S⁺⁺ ratio distribution and show high values of the η parameter, corresponding to relatively low stellar temperatures similar to high metallicity disc HII regions. This location corresponds to effective temperatures between 34700 K and 40000 K.

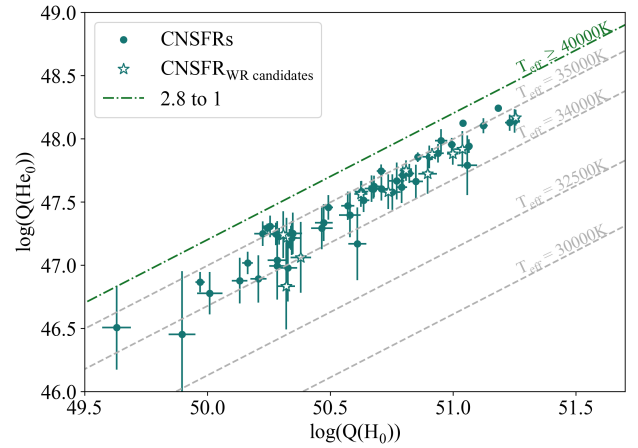
The spectral energy distribution of the ionising radiation implied by the η parameter would correspond to an ionising star cluster equivalent temperature that can be estimated from the quotient between the number of helium and hydrogen ionising photons, Q(He₀)/Q(H₀). We have calculated the number of ionising He₀ photons from the observed luminosity in the HeI λ 6678 Å emission line using the expression:

$$Q(\text{He}_0) = 1.21 \cdot 10^{49} \left(\frac{F(\text{HeI}6678)}{10^{-14}} \right) \left(\frac{D}{10} \right)^2 \quad (28)$$

where F(HeI6678), the flux of the HeI λ 6678 Å line, is expressed in erg s⁻¹ cm⁻² and D is the distance to NGC 7742 which has been taken as 22.2 Mpc (see Tab. 1). This equation has been derived using the recombination coefficient of HeI λ 6678 Å line assuming a constant value of electron density of 100 cm⁻³, a temperature of 10⁴ K and case B recombination (Osterbrock & Ferland 2006).

We have detected and measured the HeI λ 6678 Å line in 63 ring regions. The corresponding values range from 2.8 × 10⁴⁶ to 1.7 × 10⁴⁸ with a mean value of 4.5 × 10⁴⁷ photons s⁻¹.

Using the Cloudy (Ferland et al. 2013) code we have computed models with ionisation parameter values from -4.0 to -2.5, solar metallicity and a constant value of the electron density of 100 cm⁻³. The nebula is ionised by stellar atmospheres from Mihalas (1978, non-LTE models for B and O stars, log(g) = 4 and T_{eff} from 30000 K to 55000 K). For temperatures lower than 40000 K, the nebular zone of He⁺ is smaller than that of H⁺ and hence we can use the number of ionising hydrogen and helium photons to estimate the effective temperature of our ionising star clusters for which we have

**Figure 15.** Relation between the logarithmic numbers of HeI and H I ionising photons (see text for details).

derived the following equation:

$$\log \left(\frac{Q(\text{H}_0)}{Q(\text{He}_0)} \right) = (1.944 \pm 0.284) \cdot 10^{-8} \cdot T_{eff}^2 \quad (29)$$

$$(-1.527 \pm 0.199) \cdot 10^{-3} \cdot T_{eff} + (32.77 \pm 3.46)$$

This relation can be used only for logarithmic values of Q(H₀)/Q(He₀) greater than 2.8 since, for higher temperatures, the ionisation zones of helium and hydrogen coincide and the relationship between them remains constant. Fig. 15 shows the number of He₀ ionising photons as a function of the number of H₀ ionising photons. Superimposed are the lines corresponding to different temperatures as obtained with the last equation. According to these models, we can deduce that the He⁺ nebular zone is much smaller, approximately in a ratio r_{He}/r_H ~ 0.73, than that of H⁺ in all these star clusters and they seem to have similar effective temperatures, around 34600 K, a result similar with that obtained with the η parameter.

The equivalent width (EW) of Balmer lines can be understood as an estimator of the age of a young cluster single stellar population (Dottori 1981) reflecting the ratio between the present and past star formation rates. Following the notation used in Sec. 3.3, the equivalent width has been calculated as: EW(λ) = F _{λ} /(F_c(λ) + A_c(λ)). The equivalent widths of the H β emission line for the selected ring HII regions are between 2.5 to 44.0 Å with a mean

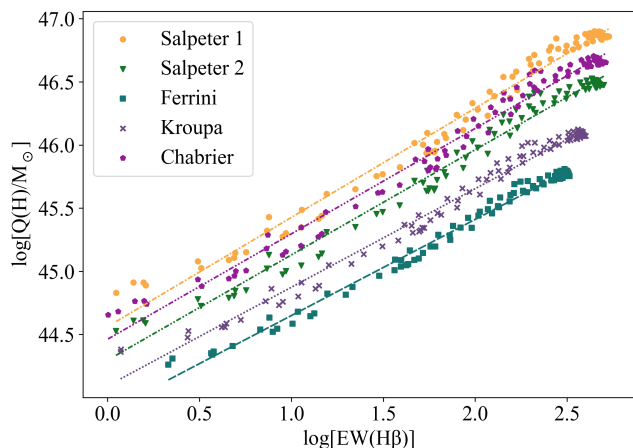


Figure 16. Linear regression between the $EW(H\beta)$ and the number of ionising photons for different IMFs according to Tab. 11 as labelled.

value of 10.9 \AA corresponding to regions of active star formation. Although the Balmer emission line luminosities are higher for ring regions, on average, the $H\beta$ equivalent widths for regions outside the ring are comparable within the errors with a mean value of 12.4 \AA covering values from 2.03 to 140.5 \AA . This might seem to point out to HII regions outside the ring being on the same evolutionary stage with similar percentages of young populations, it should be noted that the $H\beta$ equivalent width depends also on the underlying continuum and the area covered by the ring shows an additional blue population that could be affecting the results (see lower left panel of Fig. 1).

In principle, we would expect that the regions inside the ring, being closer to the galactic nucleus, were redder, with a higher metal content and with older ages (Rodríguez-Baras et al. 2018) than the regions outside the ring; however their r-i colours are comparable (see Sec. 3.4, Fig. 4). Thus, all the regions analysed in our sample seem to have similar ages and metallicities, in spite of its distance to the centre of the galaxy. In fact, this can be seen by looking at the radial r and i magnitude profiles shown by Wakamatsu et al. (1996) which follow each other.

A linear regression can be performed between the $EW(H\beta)$ and the number of ionising photons in order to estimate the ionising masses of our circumnuclear HII regions. We have used single stellar population (SSP) PopStar models (Mollá et al. 2009) to fit the following equation:

$$\log [Q(H)/M_{\odot}] = a + b \cdot \log [EW(H\beta)] \quad (30)$$

where $Q(H)/M_{\odot}$ is the total number of ionising photons per unit mass. This relation is well established for ages under 10 Ma and metallicities between 0.004 and 0.02. Its linearity can be lost: (i) for higher metallicities, because the effective temperature decreases and hence stars of the same spectral type with more metals have fewer ionising photons; (ii) for lower metallicities, because there are more massive stars and clusters are hotter, showing a significant nebular continuum; and (iii) due to the presence of Wolf Rayet (WR) stars. The slope of the initial mass function (IMF) and the lower mass limit also affect the numbers of stars of different types (and therefore their number of ionising photons). We have used the different IMFs listed in Tabé 11. Finally, we have selected ages lower than 7 Ma since, as explained above, star clusters older than that do not produce significant ionising radiation.

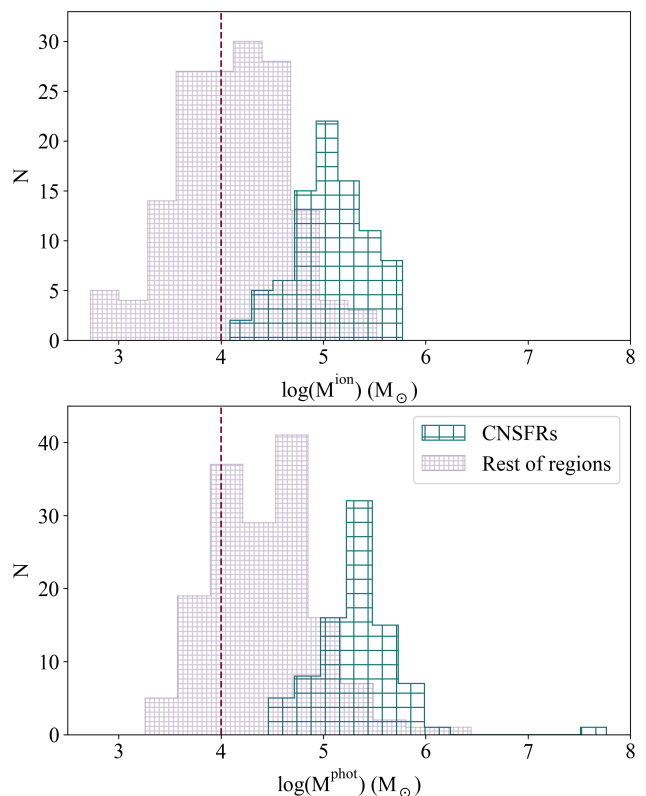


Figure 17. Histograms of the distributions of ionising masses (upper) and the photometric masses (bottom) for the ring HII regions, in green, and outside regions, in purple. The dashed line corresponds to $10^4 M_{\odot}$ (García Vargas & Díaz 1994, see text for details).

The different relations defined in Tab. 11 by equation 30 are shown in Fig. 16. The linear regression slopes are very similar among them and also compatible with previous results obtained by Díaz (1998) using stellar populations synthesis models from Cerviño & Mas-Hesse (1994), García-Vargas et al. (1995) and Leitherer & Heckman (1995). However, we can see that the linear regression intercepts differ by a factor of 5 (~ 0.7 dex) depending on the chosen IMF.

We have used the Salpeter IMF with $\phi(m) = m^{-\alpha}$, $\alpha = 2.35$, $m_{low}(M_{\odot}) = 0.85$ and $m_{up}(M_{\odot}) = 120$ that seems the most suitable for our young regions. For regions within the ring we have obtained values between 1.22×10^4 (R76) and $5.93 \times 10^5 M_{\odot}$ (R41). These results are only lower limits to the ionising masses since we are assuming that: (i) there is no dust absorption and reemission at infrared wavelengths and (ii) we are considering there is no photon escape from HII regions (but see Castellanos et al. 2002b). Our derived values are lower than those obtained by Díaz et al. (2007) for CNSFRs and slightly higher than for HII regions (Díaz et al. 2000b) both based on lower spatial resolution data ($0.4''$ and $0.7''$ respectively).

The upper panel of Fig. 17 shows the distribution of ionising masses for the ring HII regions as compared with the ones outside the ring. We can see that masses for the latter ones are an order of magnitude lower with 1.38×10^4 and 1.22×10^5 as median values respectively. Around $\sim 50\%$ of regions outside the ring have masses lower than $10^4 M_{\odot}$, hence the IFM might not be fully sampled (García Vargas & Díaz 1994; Villaverde et al. 2010). For

Table 11. Ionising masses fitting.

IMF	Reference	m_{low} (M_{\odot})	m_{up} (M_{\odot})	a	b
Salpeter1	Salpeter (1955)	0.85	120	44.561 ± 0.025	0.865 ± 0.012
Salpeter2	Salpeter (1955)	0.15	100	44.296 ± 0.024	0.833 ± 0.012
Ferrini	Ferrini et al. (1990)	0.15	100	43.887 ± 0.017	0.762 ± 0.009
Kroupa	Kroupa & Boily (2002)	0.15	100	44.092 ± 0.021	0.781 ± 0.010
Chabrier	Chabrier (2003)	0.15	100	44.461 ± 0.024	0.835 ± 0.012

the used stellar population models and the chosen IMF, the ratio of ionising stellar masses and ionised hydrogen masses, $M_{ion}/M(HII)$, takes a value of 28.

Using the same models, we have derived the photometric masses of our CNSFRs from their r -magnitudes. In this case, we cannot establish an analytical equation due to the non linearity between $\log[EW(H\beta)]$ and $M_r + 2.5 \cdot \log(M_{\odot})$. The r magnitude for $1 M_{\odot}$ seems to be constant for a chosen IMF although there are variations at ages between 3.5 and 6.5 Ma induced by the presence of WR and red super giants stars (RSG). For the regions within the ring we have obtained values between 2.90×10^4 and $1.10 \times 10^6 M_{\odot}$ corresponding to the two regions mentioned above at the extremes of ionising star masses. As expected, these latter ones show photometric masses an order of magnitude lower than the former since photometric masses follow ionising star masses in a constant proportion of about 3. An exception to this is the case of R40, that shows the highest value of the photometric mass (7.77 in the log). The physical properties of the ionising cluster are fully compatible with the rest of the ring observed regions. However, the extracted aperture encloses a non ionising star cluster. The bottom panel of Fig. 17 shows the distribution of the photometric masses for the ring HII regions as compared with the ones outside the ring.

Table 12 shows the ionising cluster properties for each HII region within the ring and lists in columns 1 to 6: (1) the region ID, (2) the logarithmic η parameter, (3) the number of helium ionising photons, (4) the measured equivalent width of $H\beta$ line, (5) the ionising mass and (6) the photometric mass.

4.5 CNSFR evolutionary stage

Up to now, we have assumed in our analysis the presence of a single population. We have checked this hypothesis by looking for the presence of a non-ionising population. In order to do that, we have constructed a pixel-to-pixel intensity profile from the 5400 and 8150 Å continuum maps (see Fig. 1) as can be seen in Fig. 18. Two populations can be clearly identified in the ring region enclosed by blue vertical lines. One of them shows up very prominently at the blue continuum wavelength. We identify this flux excess with a young non-ionising population. This is accompanied by a moderate excess of continuum flux at the redder wavelengths that might correspond to the presence of red supergiant stars. To isolate the ionising clusters' contribution, we have corrected the integrated extracted spectra for the presence of the underlying non-ionising cluster population and the galaxy disc underneath that can be fitted by a Sersic light profile. Once this has been accomplished, we have recalculated the $H\beta$ equivalent width and the r and i magnitudes assuming for the stellar population the same extinction as that of the gas.

Fig. 19 shows the relation between the logarithm of the equivalent width of the $H\beta$ line, $\log EW(H\beta)$, and the $r-i$ colour. Super-

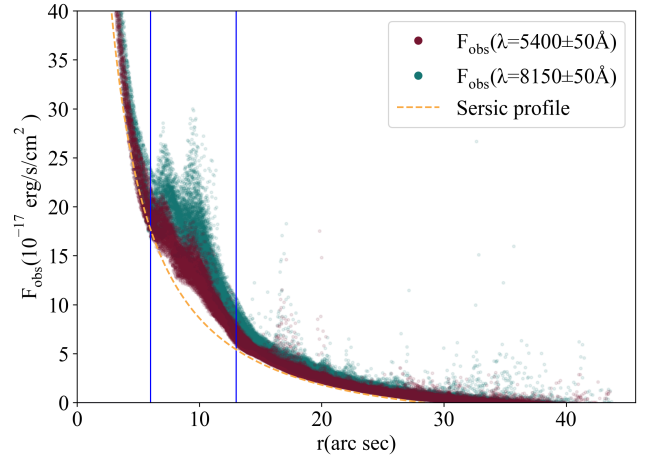


Figure 18. Observed continuum fluxes in individual spaxels as a function of radius in the blue (5400 Å) and red (8150 Å) spectral ranges. The ring limits are marked with blue vertical lines.

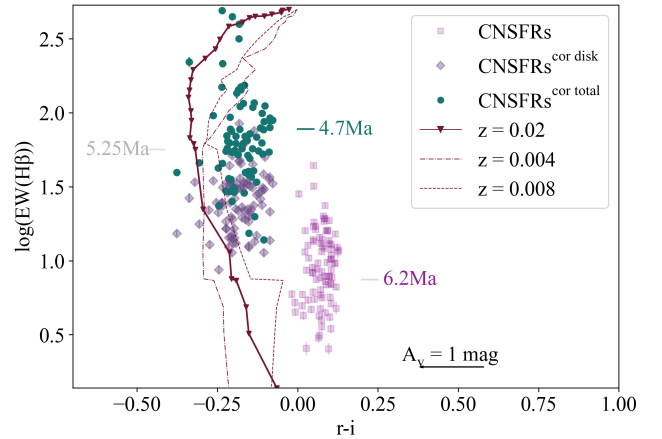


Figure 19. The relation between the equivalent width of the $H\beta$ emission line and the $r-i$ colour. The solid line has been calculated with PopStar models (Mollá et al. 2009). The beginning and end of the line correspond to ages of 0.1 and 8.5 Ma. Observational errors are inside the symbols in the graph.

imposed are single stellar population models from PopStar (Mollá et al. 2009, Salpeter's IMF, $m_{low} = 0.15 M_{\odot}$, $m_{up} = 100 M_{\odot}$). $EW(H\beta)$ can be related to the time scale of the evolution of ionising star clusters, i.e. up to 10 Ma and, for a single stellar population, decreases with age. On the other hand, the $r-i$ colour samples a

Table 12. Ionising cluster properties. The complete table is available online; here only a part is shown as an example.

Region ID	$\log(\eta)$	$Q(\text{He0})$ (photons s^{-1})	$\text{EW}(\text{H}\beta)$ (\AA)	M_{ion} (M_{\odot})	M_{phot} (M_{\odot})
R1*	1.498 ± 0.043	$(174.0 \pm 6.9) \times 10^{46}$	43.99 ± 1.60	$(15.9 \pm 1.3) \times 10^4$	$(26.3 \pm 2.2) \times 10^4$
R2	1.383 ± 0.064	$(132.7 \pm 7.7) \times 10^{46}$	31.80 ± 1.31	$(15.1 \pm 1.3) \times 10^4$	$(25.9 \pm 2.5) \times 10^4$
R3	0.992 ± 0.130	$(14.7 \pm 2.1) \times 10^{47}$	19.30 ± 0.83	$(38.2 \pm 3.3) \times 10^4$	$(66.1 \pm 8.6) \times 10^4$
R4	0.918 ± 0.100	$(75.4 \pm 8.2) \times 10^{46}$	20.07 ± 0.76	$(16.8 \pm 1.4) \times 10^4$	$(28.4 \pm 3.6) \times 10^4$
R5	1.072 ± 0.093	$(71.3 \pm 6.2) \times 10^{46}$	23.64 ± 0.99	$(12.8 \pm 1.1) \times 10^4$	$(22.8 \pm 2.4) \times 10^4$
R6	0.961 ± 0.099	$(19.6 \pm 1.6) \times 10^{46}$	28.25 ± 1.72	$(26.8 \pm 2.6) \times 10^3$	$(43.2 \pm 4.4) \times 10^3$
R7	-	$(9.0 \pm 1.1) \times 10^{47}$	17.01 ± 0.63	$(23.4 \pm 1.9) \times 10^4$	$(38.5 \pm 5.5) \times 10^4$
R8	-	$(12.7 \pm 1.7) \times 10^{47}$	16.04 ± 0.63	$(33.1 \pm 2.8) \times 10^4$	$(52.4 \pm 8.6) \times 10^4$
R9	-	$(13.4 \pm 2.0) \times 10^{47}$	15.97 ± 0.67	$(42.6 \pm 3.7) \times 10^4$	$(6.2 \pm 1.0) \times 10^5$
R10	-	$(8.7 \pm 1.1) \times 10^{47}$	18.21 ± 0.69	$(25.9 \pm 2.2) \times 10^4$	$(42.4 \pm 5.8) \times 10^4$

* Region near SN explosion.

longer time scale (≥ 300 Ma), becoming redder with age (see [Díaz et al. 2000c](#)). For this reason, this graph can be understood as an age balance between the old and young population present in our clusters.

Our observed ring regions, taken at face value (square symbols in the graph), lie to the red from the line defined by single population stellar evolution models and show rather low values of $\log \text{EW}(\text{H}\beta)$. However, relaxing the assumption of a single stellar population and correcting for the underlying disc population and young non-ionising population identified above, the data points move up and to the left in the diagram, indicating younger ages for the ionising clusters. Regarding colour correction, we can see that the regions in the galaxy disc (square symbols on the graph) have the reddest colours while both the ring non-ionising population (diamond symbols) and the isolated young ionising clusters (solid circle symbols) show similar r-i values. According to the PopStar models we are using, these colour corresponds to stellar populations of about 300 Ma. The red colours shown by the youngest stellar populations are due to the contribution by a nebular continuum of up to 50 %. On the other hand, the $\text{EW}(\text{H}\beta)$ of our ring regions, taken at face value, indicate mean ages of 6.2 Ma while the isolated young ionising population indicates younger ages with a mean value of 4.7 Ma. These latter ages are more consistent with model results than the former ones, since star clusters older than 5.2 Ma do not produce a detectable emission-line spectrum ([Martín-Manjón et al. 2010](#)). Composite young stellar populations have also been derived for CNSFRs in selected galaxies using FUV observations and a different methodology to the one described in our work ([Sirressi et al. 2022](#)).

Additionally, we have detected carbon Wolf-Rayet (WRC) star features in the spectra of some of the analysed ring HII regions. The upper panel of Fig. 20 shows the location of these regions, 15 in total, (regions R3, R4, R21, R26, R35, R36, R40, R50, R55, R56, R58, R70, R72, R78, R85; this last one was removed due to its position on the BPT diagram). The lower panel of Fig. 20 shows an example of the R3 spectrum showing the $\text{CIV}\lambda\lambda 5801, 12 \text{ \AA}$ and $\text{CIII}\lambda 5696 \text{ \AA}$ lines (see [Massey et al. 1992](#)). The presence of these features places the age of the regions between 3.2 and 5.25 Ma according to the PopStar models described above.

In order to better constrain the evolutionary stage of our CNSFRs, we have studied the evolution of the $[\text{SII}]\lambda\lambda 6717, 31 \text{ \AA} / [\text{SIII}]\lambda\lambda 9069, 9532 \text{ \AA}$ ratio with the age of our ionising regions. The $[\text{SII}]/[\text{SIII}]$ ratio is a good indicator of ionisation parameter and depends on ionising mass for zero age stellar populations and

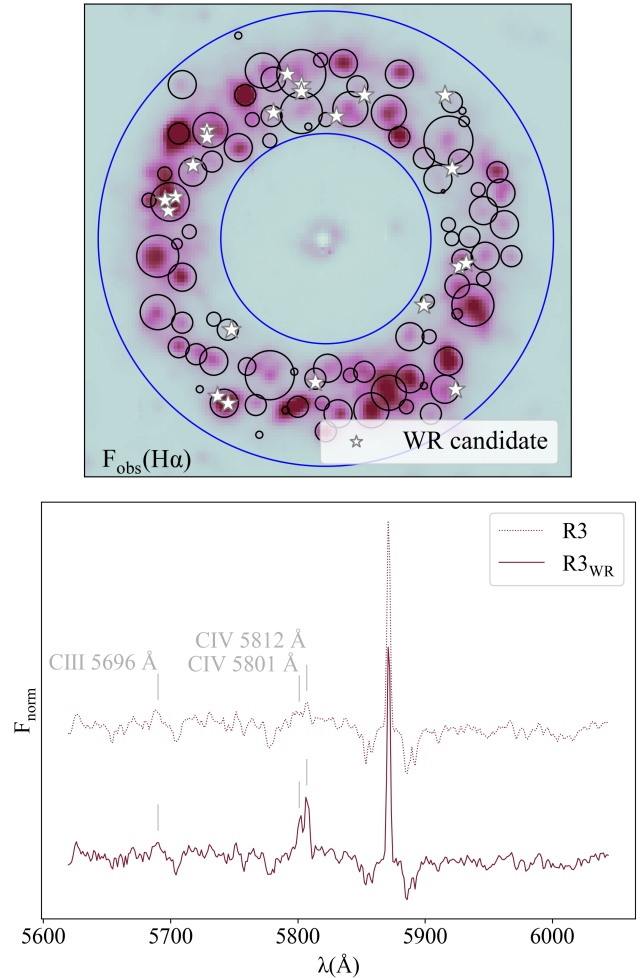


Figure 20. Upper panel: Map of the observed $\text{H}\alpha$ flux. HII regions and WR candidates are plotted with black circles and stars respectively. Orientation is North up, East to the left. The limits of the ring are marked by blue circles. Lower panel: Emission lines of WR stars in region R3 (see [Massey et al. 1992](#)). Dashed and solid lines correspond to the integrated spectrum and the spectrum of areas showing the WR features respectively.

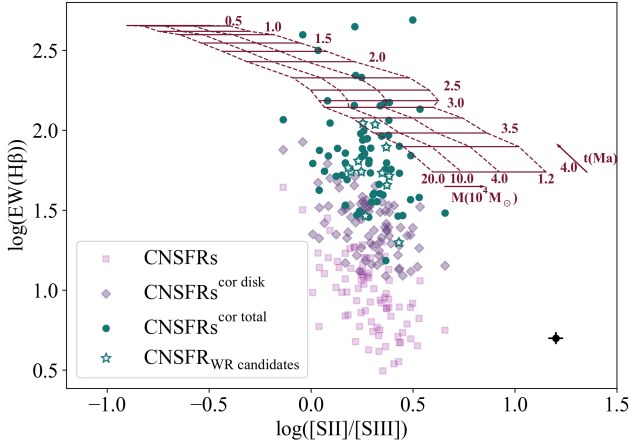


Figure 21. The relation between the equivalent width of the $H\beta$ emission line and the $[SII]\lambda\lambda 6717,31 \text{ \AA} / [SIII]\lambda\lambda 9069,9532 \text{ \AA}$ ratio. Solid and dashed lines are from PopStar models with Cloudy and metallicity $z = 0.02$ (Martín-Manjón et al. 2010; García-Vargas et al. 2013). Mean error bars for CNSFRs are shown at the bottom right corner of the panel.

then decreases as the cluster evolves due to the increasing loss of ionising photons.

Fig. 21 shows the relation between the equivalent width of the $H\beta$ emission line and the $[SII]/[SIII]$ ratio. Superimposed are the same solar metallicity PopStar models used before. A trend between the degree of evolution and the degree of ionisation of the nebula seems to exist in the galaxy disc population (magenta squares in the graph). This effect was already noticed by Hoyos & Díaz (2006) being explained by the different contributions of continuum light from underlying populations. The IFU data analysed here allow the subtraction of the disc and the young non-ionising stellar populations. Once this has been done, this trend is lost and the isolated young ionising clusters appear to cover the area occupied by the models. Furthermore, the CNSFRs with WR features are concentrated in a narrow range of ages around 3.5 Ma in agreement with the single stellar population models used.

This correction also affects our initially derived ionising cluster masses and the photometric masses quoted in Section 4.4, through the number of ionising photons per unit solar mass which depends on $EW(H\beta)$ for the former and the r -magnitude for the latter. The corrected values of the ionising cluster masses have a mean of $3.5 \times 10^4 M_{\odot}$, a factor of about 4.5 smaller than uncorrected ones; in the case of the photometric masses the corrected mean value is $1.8 \times 10^5 M_{\odot}$. This gives a ratio of ionising cluster mass to photometric mass of about 19 %.

5 CONCLUSIONS

In this work we present a study of the physical properties of the CNSFRs in the ring of the face-on spiral NGC 7742 using MUSE observations publicly available and the full spectral region observed, from 4800 to 9300 \AA . The work is centred in the study of the individual ionising clusters that power the HII regions populating the ring of the galaxy. We have used the data cubes from the ESO Science Archive to produce 2D maps in the $H\alpha$ and $H\beta$ emission lines obtaining the spatial distribution of the visual extinction necessary for the nebular analysis. Additionally, two continuum maps at central wavelengths 5400 and 8150 \AA and the line maps of [OIII] and

[NII] are also presented. A map of the $EW(H\alpha)$ emission shows the circumnuclear regions within the ring, object of this study, having $EW(H\alpha) > 20 \text{ \AA}$, consistent with the presence of star formation occurred less than 10 Ma ago. We have delimited the ring from the radial distribution of the observed $H\alpha$ flux, as having an inner radius of 6 arcsec (0.75 kpc) and an outer radius of 13 arcsec (1.63 kpc). The observed $H\alpha$ flux map has been used to select the ring ionised regions and also a set of HII regions external to it for comparison purposes. At the end of the procedure, we have obtained a total of 88 HII regions in the ring and 158 regions outside. The emission line ratios of the HII regions within the ring are consistent with the predictions of star forming models. However, maps of the central part of NGC 7742 in the [OIII] and [NII] emission line ratios allow the identification of a small circumnuclear ring at about 200 pc from the galaxy nucleus that seems to be dominated by shocks or an AGN non-thermal component of low activity. Three of our segmented ring regions to the South-East, R85, R86 and R87 may be somewhat affected by the radiation from the galaxy nucleus and consequently, they have not been considered in our analysis.

In order to study the properties of the selected CNSFRs, we have measured the most prominent emission lines in their spectra: $H\beta$ and $H\alpha$ Balmer lines; [OIII] $\lambda\lambda 4959,5007 \text{ \AA}$, [NII] $\lambda\lambda 6548,84 \text{ \AA}$, [SII] $\lambda\lambda 6716,31 \text{ \AA}$, [ArIII] $\lambda 7136 \text{ \AA}$ and [SIII] $\lambda 9069 \text{ \AA}$ forbidden lines and also the weaker lines of [SIII] $\lambda 6312 \text{ \AA}$, HeI $\lambda 6678 \text{ \AA}$ and [OII] $\lambda\lambda 7320,30 \text{ \AA}$. We have calculated as well integrated fluxes inside the Sloan Digital Sky Survey (SDSS) filters for each selected region by convolving the appropriate filter transmission with their spectral energy distributions. A colour-magnitude diagram $r-i$ vs M_r shows the CNSFRs to have a rather constant value.

For our observed ring HII regions we have derived: (1) the number of Hydrogen ionising photons per second, $Q(H_0)$; (2) the electron density of the emitting gas per cubic centimeter, n_e ; (3) the ionisation parameter, u ; (4) the corresponding angular radius in arcsec; (5) the filling factor; and (6) the mass of ionised hydrogen in solar masses, $M(HII)$. All these values are consistent with those found in other studies of similar regions. $Q(H_0)$ is between 2.57×10^{49} and 1.51×10^{51} which points to these regions being ionised by star clusters; the electron density of the ionised gas is well below the critical one for collisional deexcitation; the ionisation parameter is inside a narrow range centred around $\log(u) \approx -3.5$; the estimated angular radii are in very good agreement with the measured ones, all of them spatially resolved, and show linear values between 34 and 130 pc; filling factors are low, with a mean value of 0.043, similar to the ones estimated for high metallicity disc HII regions; and, finally, the ionised hydrogen mass has a mean value of $3.07 \times 10^4 M_{\odot}$.

We have used sulphur as a tracer for chemical abundances of the selected HII regions using the methodology developed in Díaz & Zamora (2022), very adequate to the spectral characteristics of the MUSE spectroscopic data: 4800-9300 \AA wavelength range and spectral dispersion of 1.25 $\text{\AA}/\text{pix}$ and the expected abundances of the studied regions, in the high metallicity range. The weak, temperature sensitive [SIII] $\lambda 6312 \text{ \AA}$ line has been measured with a S/N higher than 1 in $\sim 45 \%$ (38 out of 88) of the HII regions within the ring. For these regions total sulphur abundances have been derived by the so called "direct method". For the rest of the regions we had to rely on empirical calibrations to derive their sulphur abundances, which has been done through the use of the S_{23} parameter that has little dependence on reddening effects or calibration uncertainties since the lines involved can be measured relative to nearby hydrogen recombination lines. Also, the lines are observable even at over-solar abundances given their lower dependence with elec-

tron temperature. Derived sulphur abundances are between $6.53 \leq 12+\log(S/H) \leq 7.50$, that is between 0.25 and 2.4 times the solar value, with most regions showing values slightly below solar. For a few ring HII regions we derived the total oxygen abundances using the [OII] $\lambda\lambda$ 7220,30 Å to calculate the O⁺ contribution. For three of the analysed regions oxygen abundances are found to be high, of the order of $12+\log(O/H)$ around 9.0 (2 times solar) with a contribution by O⁺ to the total abundance as high as 90 %. These values reflect in very low S/O ratios. Similar values have been found for other high metallicity regions by different authors.

The final part of this work concerns the properties of the CNSFR ionising clusters. For the regions presenting the [OII] $\lambda\lambda$ 7220,30 Å lines we derived the η parameter that can be related to the effective temperature of the ionising radiation, finding values close to $\log(\eta)$ around 1.0, which implies low effective temperatures. An equivalent temperature of the ionised clusters can be estimated from the ratio of helium to hydrogen ionising photons, $Q(\text{He}_0)/Q(\text{H}_0)$. For 63 regions we could derive this ratio using the HeI λ 6678 Å line finding a rather constant value of around 10^{-3} , corresponding to an equivalent temperature below 40000 K. The masses of ionising clusters, once corrected for the contribution of underlying non-ionising populations, were derived using PopStar models and are found to have a mean value of $3.5 \times 10^4 M_\odot$, comparable to the mass of ionised gas and about 19 % of the corrected photometric mass. The young stellar population of the CNSFRs has contributions of ionising and non-ionising populations in a ratio 0.24 with ages around 5 Ma and 300 Ma respectively.

The homogeneity of abundances and continuum colours, together with the kinematics and counter rotating nature of the ring fits the minor merger scenario proposed by previous works. This merger would have triggered the star formation in the ring producing massive star clusters showing at present a young stellar population 300 Ma old accompanied by a subsequent young ionising population involving around 20 % of the integrated cluster masses. Satellite accretion and major or minor mergers have also been suggested as the origin of the galaxy clumps observed at intermediate redshift (see e.g. Elmegreen & Elmegreen 2005). However, a recent study of clumps and accreted satellites in 53 star forming galaxies at $z \sim 1-3$ (Zanella et al. 2019) shows that, although the more extended clumps are probably formed in merger processes, the identified compact clumps formed *in situ* show physical properties: sizes ($\sim 1-2$ Kpc), masses ($\sim 10^7-10^8 M_\odot$), ages ≤ 10 Ma and metallicities ($12+\log(O/H) \approx 8.56$), more compatible with the total values found for the ensemble of ionising clusters studied here, as it would be observed at the quoted redshift. Obviously, more data, preferably at low to intermediate redshift, are needed in order to distinguish between these two hypotheses.

ACKNOWLEDGEMENTS

This research has made use of the services of the ESO Science Archive Facility and NASA's Astrophysics Data System Abstract Service. It is based on observations collected at the European Organisation for Astronomical Research in the Southern Hemisphere under ESO programme 60.A-9301(A) and data products created thereof. Also we have used observations obtained with the NASA/ESA HST and obtained from the Hubble Legacy Archive, which is a collaboration between the Space Telescope Science Institute (STScI/NASA), the Space Telescope European Coordinating Facility (ST-ECF/ESA), and the Canadian Astronomy Data Centre (CAD/C/NRC/CSA).

This work has been supported by Spanish grants from the former Ministry of Economy, Industry and Competitiveness through the MINECO-FEDER research grant AYA2016-79724-C4-1-P, the present Ministry of Science and Innovation through research grant PID2019-107408GB-C42 and the National Research Agency through research grant AEI/10.13039/501100011033.

S.Z. acknowledges the support from contract: BES-2017-080509 associated to the first of these grants.

DATA AVAILABILITY

The original data on which this article is based can be found in the ESO Science Archive Facility from ESO telescopes at La Silla Paranal Observatory.

REFERENCES

- Aggarwal K. M., Keenan F. P., 1999, *ApJS*, **123**, 311
- Álvarez-Álvarez M., Díaz A. I., Terlevich E., Terlevich R., 2015, *MNRAS*, **451**, 3173
- Asplund M., Grevesse N., Sauval A. J., Scott P., 2009a, *ARA&A*, **47**, 481
- Asplund M., Grevesse N., Sauval A. J., Scott P., 2009b, *ARA&A*, **47**, 481
- Bacon R., et al., 2010, The MUSE second-generation VLT instrument. p. 773508, doi:10.1117/12.856027
- Baldwin J. A., Phillips M. M., Terlevich R., 1981, *PASP*, **93**, 5
- Bregman J. N., Houck J. C., Chevalier R. A., Roberts M. S., 2003, *ApJ*, **596**, 323
- Bresolin F., Schaerer D., González Delgado R. M., Stasińska G., 2005, *A&A*, **441**, 981
- Castellanos M., Díaz A. I., Terlevich E., 2002a, *MNRAS*, **337**, 540
- Castellanos M., Díaz A. I., Tenorio-Tagle G., 2002b, *The Astrophysical Journal*, **565**, L79
- Cedrés B., Beckman J. E., Bongiovanni Á., Cepa J., Asensio Ramos A., Giammanco C., Cabrera-Lavers A., Alfaro E. J., 2013, *ApJ*, **765**, L24
- Cerviño M., Mas-Hesse J. M., 1994, *A&A*, **284**, 749
- Chabrier G., 2003, *PASP*, **115**, 763
- Christensen T., Petersen L., Gammelgaard P., 1997, *A&A*, **322**, 41
- Cid Fernandes R., Stasińska G., Schlickmann M. S., Mateus A., Vale Asari N., Schoenell W., Sodré L., 2010, *MNRAS*, **403**, 1036
- Colina L., Gonzalez Delgado R., Mas-Hesse J. M., Leitherer C., 2002, *ApJ*, **579**, 545
- Comerón S., Knapen J. H., Beckman J. E., Laurikainen E., Salo H., Martínez-Valpuesta I., Buta R. J., 2010, *MNRAS*, **402**, 2462
- Díaz Á. I., 1998, *Ap&SS*, **263**, 143
- Díaz Á. I., Zamora S., 2022, *MNRAS*, **511**, 4377
- Díaz A. I., Pagel B. E. J., Wilson I. R. G., 1985, *MNRAS*, **212**, 737
- Díaz A. I., Terlevich E., Vilchez J. M., Pagel B. E. J., Edmunds M. G., 1991, *MNRAS*, **253**, 245
- Díaz A. I., Álvarez M. Á., Terlevich E., Terlevich R., Sánchez Portal M., Aretxaga I., 2000a, *MNRAS*, **311**, 120
- Díaz A. I., Castellanos M., Terlevich E., Luisa García-Vargas M., 2000b, *MNRAS*, **318**, 462
- Díaz A. I., Castellanos M., Terlevich E., Luisa García-Vargas M., 2000c, *MNRAS*, **318**, 462
- Díaz Á. I., Terlevich E., Castellanos M., Hägele G. F., 2007, *MNRAS*, **382**, 251
- Dottori H. A., 1981, *Ap&SS*, **80**, 267
- Elmegreen B. G., Elmegreen D. M., 2005, *ApJ*, **627**, 632
- Ferland G. J., et al., 2013, *Rev. Mex. Astron. Astrofis.*, **49**, 137
- Ferrini F., Palla F., Penco U., 1990, Fragmentation Theories and the IMF. p. 357, doi:10.1007/978-94-009-0605-1_31
- Filippenko A. V., Matheson T., 1993, *IAU Circ.*, **5842**, 2
- Fukugita M., Shimasaku K., Ichikawa T., 1995, *PASP*, **107**, 945
- Galbany L., et al., 2016a, *MNRAS*, **455**, 4087
- Galbany L., et al., 2016b, *A&A*, **591**, A48

- García Vargas M. L., Díaz A. I., 1994, *ApJS*, **91**, 553
- García-Vargas M. L., Bressan A., Díaz A. I., 1995, *A&AS*, **112**, 13
- García-Vargas M. L., Mollá M., Martín-Manjón M. L., 2013, *MNRAS*, **432**, 2746
- Garnett D. R., 1992, *AJ*, **103**, 1330
- Garnett D. R., 2002, arXiv e-prints, [pp astro-ph/0211148](https://arxiv.org/abs/astro-ph/0211148)
- Gonzalez-Delgado R. M., Perez E., 1997, in Franco J., Terlevich R., Serrano A., eds, *Revista Mexicana de Astronomía y Astrofísica Conference Series Vol. 6*, *Revista Mexicana de Astronomía y Astrofísica Conference Series*. p. 264
- Gonzalez-Delgado R. M., et al., 1994, *ApJ*, **437**, 239
- Gonzalez-Delgado R. M., Perez E., Díaz A. I., García-Vargas M. L., Terlevich E., Vilchez J. M., 1995, *ApJ*, **439**, 604
- Hägele G. F., Pérez-Montero E., Díaz Á. I., Terlevich E., Terlevich R., 2006, *MNRAS*, **372**, 293
- Hägele G. F., Díaz Á. I., Cardaci M. V., Terlevich E., Terlevich R., 2007, *MNRAS*, **378**, 163
- Hägele G. F., Díaz Á. I., Terlevich R., Terlevich E., Bosch G. L., Cardaci M. V., 2013, *MNRAS*, **432**, 810
- Ho L. C., Filippenko A. V., Sargent W. L. W., 1997, *ApJS*, **112**, 315
- Hoyos C., Díaz A. I., 2006, *MNRAS*, **365**, 454
- Hudson C. E., Ramsbottom C. A., Scott M. P., 2012, *ApJ*, **750**, 65
- Jenkins E. B., 2009, *ApJ*, **700**, 1299
- Kauffmann G., et al., 2003, *MNRAS*, **346**, 1055
- Kehrig C., Vilchez J. M., Telles E., Cuisinier F., Pérez-Montero E., 2006, *A&A*, **457**, 477
- Kewley L. J., Dopita M. A., Sutherland R. S., Heisler C. A., Trevena J., 2001, *ApJ*, **556**, 121
- Kroupa P., Boily C. M., 2002, *MNRAS*, **336**, 1188
- Leitherer C., Heckman T. M., 1995, *ApJS*, **96**, 9
- Liu X. W., Luo S. G., Barlow M. J., Danziger I. J., Storey P. J., 2001, *MNRAS*, **327**, 141
- Liu X., Shapley A. E., Coil A. L., Brinchmann J., Ma C.-P., 2008, *ApJ*, **678**, 758
- Lopez L. A., Krumholz M. R., Bolatto A. D., Prochaska J. X., Ramirez-Ruiz E., 2011, *ApJ*, **731**, 91
- Luridiana V., Morisset C., Shaw R. A., 2015, *A&A*, **573**, A42
- Martín-Manjón M. L., García-Vargas M. L., Mollá M., Díaz A. I., 2010, *MNRAS*, **403**, 2012
- Martinsson T. P. K., Sarzi M., Knapen J. H., Coccato L., Falcón-Barroso J., Elmegreen B. G., de Zeeuw T., 2018, *A&A*, **612**, A66
- Massey P., Armandroff T. E., Conti P. S., 1992, *AJ*, **103**, 1159
- Mazzuca L. M., Sarzi M., Knapen J. H., Veilleux S., Swaters R., 2006, *ApJ*, **649**, L79
- Mazzuca L. M., Knapen J. H., Veilleux S., Regan M. W., 2008, *ApJS*, **174**, 337
- McGaugh S. S., 1991, *ApJ*, **380**, 140
- Mihalas D., 1978, *Stellar atmospheres*
- Miller J. S., Mathews W. G., 1972, *ApJ*, **172**, 593
- Mollá M., García-Vargas M. L., Bressan A., 2009, *MNRAS*, **398**, 451
- Nishimura K., 2014, *Central Bureau Electronic Telegrams*, **3964**, 1
- Osterbrock D. E., Ferland G. J., 2006, *Astrophysics of gaseous nebulae and active galactic nuclei*
- Pastoriza M. G., Dottori H. A., Terlevich E., Terlevich R., Díaz A. I., 1993, *MNRAS*, **260**, 177
- Pérez-Montero E., 2017, *PASP*, **129**, 043001
- Pérez-Montero E., Díaz A. I., 2005, *MNRAS*, **361**, 1063
- Pilyugin L. S., Thuan T. X., Vilchez J. M., 2006, *MNRAS*, **367**, 1139
- Pizzella A., Corsini E. M., Vega Beltrán J. C., Bertola F., 2004, *A&A*, **424**, 447
- Podobedova L. I., Kelleher D. E., Wiese W. L., 2009, *Journal of Physical and Chemical Reference Data*, **38**, 171
- Pradhan A. K., Montenegro M., Nahar S. N., Eissner W., 2006, *MNRAS*, **366**, L6
- Rodríguez-Baras M., Díaz A. I., Rosales-Ortega F. F., Sánchez S. F., 2018, *A&A*, **609**, A102
- Rodríguez-Baras M., Díaz A. I., Rosales-Ortega F. F., 2019, *A&A*, **631**, A23
- Salpeter E. E., 1955, *ApJ*, **121**, 161
- Sánchez S. F., et al., 2012, *A&A*, **546**, A2
- Sánchez S. F., et al., 2015, *A&A*, **574**, A47
- Schawinski K., Thomas D., Sarzi M., Maraston C., Kaviraj S., Joo S.-J., Yi S. K., Silk J., 2007, *MNRAS*, **382**, 1415
- Shields G. A., Searle L., 1978, *ApJ*, **222**, 821
- Sil'chenko O. K., Moiseev A. V., 2006, *AJ*, **131**, 1336
- Sirressi M., et al., 2022, *AJ*, **164**, 208
- Skrutskie M. F., et al., 2006, *AJ*, **131**, 1163
- Stasińska G., 2005, *A&A*, **434**, 507
- Storey P. J., Hummer D. G., 1995, *MNRAS*, **272**, 41
- Storey P. J., Zeppen C. J., 2000, *MNRAS*, **312**, 813
- Tayal S. S., 2007, *The Astrophysical Journal Supplement Series*, **171**, 331
- Tayal S. S., Zatsarinny O., 2010, *ApJS*, **188**, 32
- Tosi M., 1988, *A&A*, **197**, 33
- Treffers R. R., Leibundgut B., Filippenko A. V., Richmond M. W., 1993, *IAU Circ.*, **5812**, 1
- Tully R. B., Fisher J. R., 1988, *Catalog of Nearby Galaxies*
- Vacca W. D., Garmany C. D., Shull J. M., 1996, *ApJ*, **460**, 914
- Vermeij R., van der Hulst J. M., 2002, *A&A*, **391**, 1081
- Vilchez J. M., Pagel B. E. J., 1988, *MNRAS*, **231**, 257
- Villaverde M., Cerviño M., Luridiana V., 2010, *A&A*, **522**, A49
- Wakamatsu K., Hamabe M., Nishida M. T., Tomita A., 1996, in Buta R., Crocker D. A., Elmegreen B. G., eds, *Astronomical Society of the Pacific Conference Series Vol. 91*, *IAU Colloq. 157: Barred Galaxies*. p. 83
- Weilbacher P. M., Streicher O., Urrutia T., Pécontal-Rousset A., Jarno A., Bacon R., 2014, in Manset N., Forshay P., eds, *Astronomical Society of the Pacific Conference Series Vol. 485*, *Astronomical Data Analysis Software and Systems XXIII*. p. 451 ([arXiv:1507.00034](https://arxiv.org/abs/1507.00034))
- Wiese W. L., Fuhr J. R., Deters T. M., 1996, *Atomic transition probabilities of carbon, nitrogen, and oxygen: a critical data compilation*
- Zanella A., et al., 2019, *MNRAS*, **489**, 2792
- Zeppen C. J., 1982, *MNRAS*, **198**, 111
- de Zeeuw P. T., et al., 2002, *MNRAS*, **329**, 513